photonics

MDPI

Article

Dependence of the Michelson Interferometer-Based Membrane-Less Optical Microphone–Photoacoustic Spectroscopy Gas-Sensing Method on the Fundamental Parameters of a Photoacoustic Gas Cell

Shuchao Wang [1,*], Ali K. Yetisen [2], Kun Wang [1], Martin Jakobi [1] and Alexander W. Koch [1]

[1] Institute for Measurement Systems and Sensor Technology, Department of Electrical and Computer Engineering, School of Computation, Information and Technology, Technical University of Munich, 80333 Munich, Germany
[2] Department of Chemical Engineering, Imperial College London, London SW7 2AZ, UK
* Correspondence: shuchao.wang@tum.de

Abstract: This article presents a mathematical model of the Michelson interferometer (MI)-based membrane-less optical microphone (MeoM)–photoacoustic spectroscopy (MeoM–PAS) method, which is also referred to as MI-based photoacoustic interferometry (PAI), for gas-sensing applications in complex and adverse environments, as it offers a completely static measurement system and the separation of a photoacoustic (PA) gas cell from the measuring system. It also investigates the dependence of this method on the fundamental parameters of a cubical PA gas cell using axial PA signals. The results indicate that the phase of the method is a sine function of the distance between the two light beams and a power exponent of the cell length, the cell height, and the distance between the excitation source and the nearest light beam, under the condition that the PA gas cell is resonant and that the excitation source is at the position of the peak or valley of the PA signals. It is at its maximum when the distance between the two light beams is approximately half the wavelength of the PA signals under the same conditions. In addition, the dependence of a PA gas cell using non-axial PA signals is described under the conditions that the PA gas cell is resonant, which is consistent with the changing aforementioned parameters for the distance between the two light beams, the cell length and height, and the distance between the excitation source and the nearest light beam. Furthermore, the selection of five common materials (aluminum, brass, glass, quartz, and stainless steel) for the PA gas cell is discussed under the influence of temperature fluctuations outside the PA gas cell, noise inside and outside the PA gas cell, as well as thermal and viscous losses inside the PA gas cell. The results indicate that quartz and stainless steel are promising options. Finally, the parameters related to the sensitivity enhancement of the method are analyzed using mathematical models, where the sensitivity of the method can be theoretically enhanced by reducing the dimensions of the PA gas cell.

Keywords: Michelson interferometer; membrane-less optical microphone (MeoM)–photoacoustic spectroscopy (MeoM–PAS); photoacoustic interferometry (PAI); gas sensing; photoacoustic gas cell

Citation: Wang, S.; Yetisen, A.K.; Wang, K.; Jakobi, M.; Koch, A.W. Dependence of the Michelson Interferometer-Based Membrane-Less Optical Microphone–Photoacoustic Spectroscopy Gas-Sensing Method on the Fundamental Parameters of a Photoacoustic Gas Cell. *Photonics* **2023**, *10*, 888. https://doi.org/10.3390/photonics10080888

Received: 2 June 2023
Revised: 19 July 2023
Accepted: 25 July 2023
Published: 1 August 2023

1. Introduction

Optical sensing technologies are widely used to detect gas concentrations in harsh environments that involve high temperatures, high pressure, strong electromagnetic interference, and corrosive chemicals due to their non-magnetic saturation and immunity to electromagnetic interference [1]. Among all types of optical sensing methods, photoacoustic spectroscopy (PAS)-based sensing methods are the preferred approach because they have no significant drawbacks compared to other optical sensing technologies [2,3]. This technology allows for the detection of homo-nuclear diatomic gases and results in smaller and more sensitive sensors, as the limit of detection (LOD) of PAS is not fully determined

by the length of the light-gas interaction [2]. These properties enable PAS-based gas sensing methods to seamlessly function in harsh environments [4].

The optical interferometer-based technology is one of the most mainstream PAS-based gas sensing methods [2,5] due to its high sensitivity and simple structure and principle [6]. However, this method is not suitable for some harsh environments [2–5] because many current mainstream gas sensors based on the technology have movable components, such as diaphragms [7–10] and cantilever beams [11–14]. Hence, they are unsuitable for high-temperature and high-pressure applications [1–5]. Therefore, it is essential to develop optical interferometer-based gas sensing methods based on PAS without any movable components.

In this work, a mathematical model of the Michelson interferometer (MI)-based membrane-less optical microphone (MeoM)–photoacoustic spectroscopy (MeoM–PAS) gas-sensing method, also known as MI-based Photoacoustic Interferometry (PAI), is presented. It provides a completely static measurement system and the separation of a photoacoustic (PA) gas cell from the measuring system for applications in harsh environments. The dependence of this method on the fundamental parameters of a PA gas cell, including the distance between the two light beams, the cell length, the cell height, and the distance between the excitation source and the nearest light beam, is investigated using axial PA signals, under the condition that the PA gas cell is resonant and that the excitation source is at the position of the peak or valley of the PA signals. The dependence of a PA gas cell is described using non-axial PA signals, under the condition that the PA gas cell is resonant. Furthermore, the selection of five common materials used to produce PA gas cells is discussed, including aluminum, brass, glass, quartz, and stainless steel, under the influence of temperature fluctuations outside the PA gas cell, and noise inside and outside the PA gas cell, as well as thermal and viscous losses inside the PA gas cell. Finally, the parameters that influence the sensitivity of the gas-sensing method are outlined using mathematical models.

2. Mathematical Model and Theory

In Figure 1a, Schematic (1) shows the working principle [2,15] of the Michelson interferometer (MI). A light source emits a light beam, which is split into two beams, 1 and 2, by a beam splitter. When the refractive index of the medium at the position of one beam varies, a difference in the optical path can be formed between the two beams. Interference occurs when these two beams of light are reflected by two flat mirrors and then meet again. The relationship [15,16] between phase $\Phi_{MI}(t)$ and the output light intensity $I_{MI}(\Phi_{MI}(t))$ (unit: W/m^2) in the MI is shown in Equation (1).

$$I_{MI}(\Phi_{MI}(t)) = I_1 + I_2 + 2\sqrt{I_1 I_2}\cos(\Phi_{MI}(t)). \quad (1)$$

In Equation (1), I_1 represents the light intensity of light beam 1 in the MI (unit: W/m^2); I_2 shows the light intensity of light beam 2 in the MI (unit: W/m^2), and t indicates time (unit: s).

Assuming that the lengths of the two beam paths in the MI are equal, the intensities of the two beams are equal: $I_1 = I_2 = I_0$. Therefore,

$$I_{MI}(\Phi_{MI}(t)) = 2I_0\,(1 + \cos(\Phi_{MI}(t))). \quad (2)$$

The relationship [16,17] between phase $\Phi_{MI}(t)$ and the refractive indices, $n_1(t)$ and $n_2(t)$, at the two beam positions in the MI is shown in Equation (3).

$$\Phi_{MI}(t) = \frac{4\pi L_{LB}}{\lambda}\,(n_1(t) - n_2(t)). \quad (3)$$

In Equation (3), L_{LB} represents the length of the two light beams in the MI (unit: m) and λ is the wavelength of the incident light (unit: m).

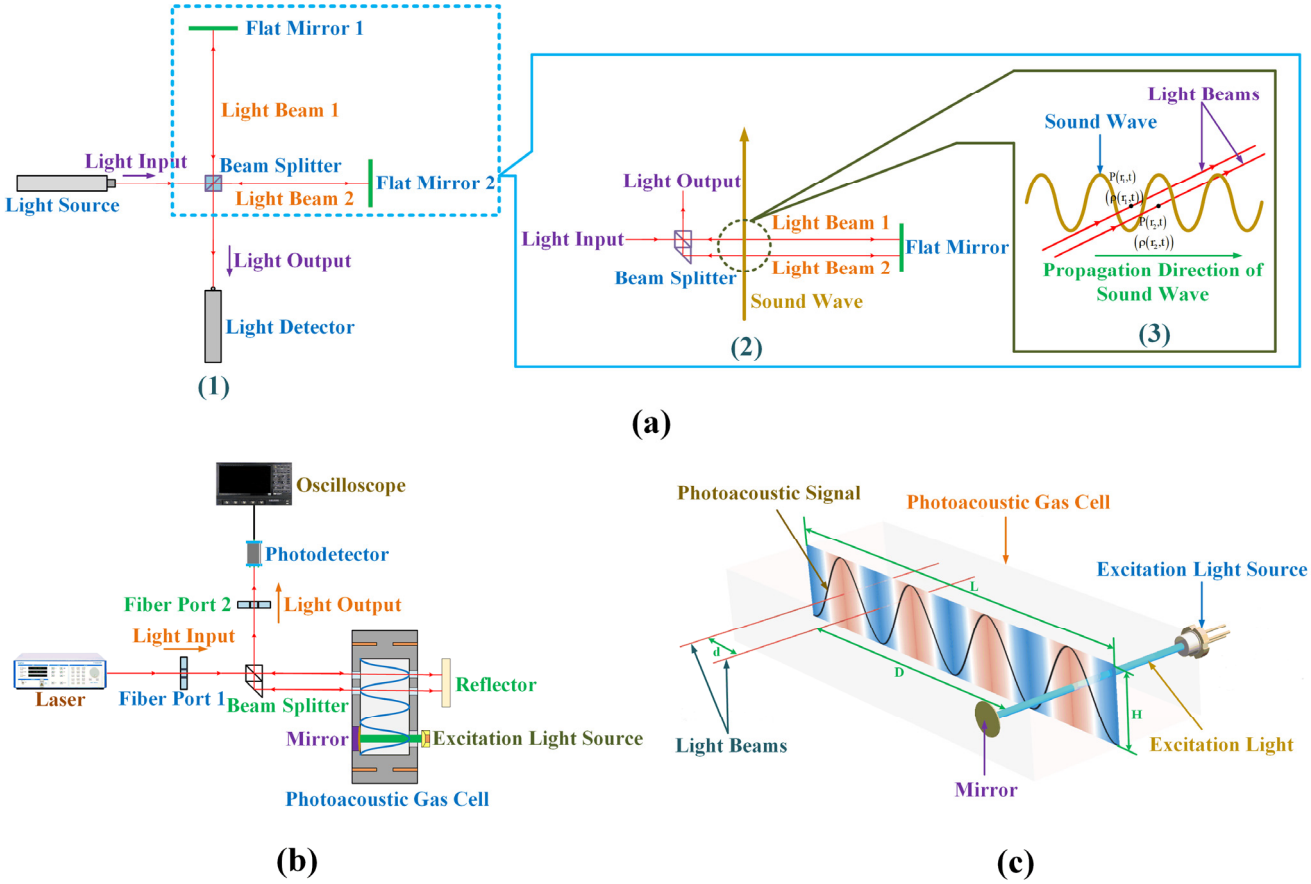

Figure 1. (**a**) Schematic of the working principles of the MI and the MI-based MeoM in sensing sound waves and gas concentrations: (1) the MI; (2) the MI-based MeoM in sensing sound waves; and (3) the MI-based MeoM in sensing gas concentrations. (**b**) Schematic of the sensing principle for the MI-based MeoM–PAS gas-sensing method. (**c**) Dependency exploration of the MI-based MeoM–PAS gas-sensing method on the fundamental parameters of a PA gas cell.

Sound waves are variations in gas pressure that oscillate around a static ambient pressure [18,19]. Therefore, the total pressure caused by the sound waves $P_{total}(r, t)$ (unit: Pa) is the sum of the gas pressure generated by the sound waves $P(r, t)$ (unit: Pa) and the ambient pressure $P_{ambient}$ (unit: Pa):

$$P_{total}(r, t) = P_{ambient} + P(r, t). \quad (4)$$

In Equation (4), r represents the position and t is the time (unit: s).

The MI can be used as a MeoM to sense sound waves [2]. Therefore, when sound waves pass vertically through the two beam paths in the MI (Schematic (2) in Figure 1a), it is assumed that the ambient pressure $P_{ambient}$, the Celsius temperature T (unit: °C), and the relative humidity in percent RH [20] are the same for the two beam paths in the MI. Then, the difference in refractive indices in the MI, $n_1(t) - n_2(t)$, can be directly obtained from the Edlen Formula [21,22] and the simplified correction formula provided by the National Institute of Standards and Technology (NIST) based on the Edlen Formula [23,24].

$$n_1(t) - n_2(t) = \left[1 + 7.86 \times 10^{-4} \frac{P_{total}(r_1, t)}{273 + T} - 1.5 \times 10^{-11} RH \left(T^2 + 160\right)\right],$$

$$-\left[1 + 7.86 \times 10^{-4} \frac{P_{total}(r_2, t)}{273 + T} - 1.5 \times 10^{-11} RH \left(T^2 + 160\right)\right],$$

$$= \left[1 + 7.86 \times 10^{-4} \frac{(P_{ambient} + P(r_1, t))}{273 + T} - 1.5 \times 10^{-11} RH \left(T^2 + 160\right)\right],$$

$$- \left[1 + 7.86 \times 10^{-4} \frac{(P_{ambient} + P(r_2, t))}{273 + T} - 1.5 \times 10^{-11} RH \left(T^2 + 160\right)\right]. \quad (5)$$

In Equation (5), $P_{total}(r_1, t)$ represents the total pressure caused by the sound waves at the position of the light beam 1 in the MI (unit: Pa); $P_{total}(r_2, t)$ shows the total pressure caused by the sound waves at the position of the light beam 2 in the MI (unit: Pa); $P(r_1, t)$ indicates the gas pressure generated by the sound waves at the position of the light beam 1 in the MI (unit: Pa); and $P(r_2, t)$ is the gas pressure generated by the sound waves at the position of the light beam 2 in the MI (unit: Pa).

Therefore, the difference in refractive indices at the positions of the two light beams in the MI, $n_1(t) - n_2(t)$, can be expressed as:

$$n_1(t) - n_2(t) = \frac{\delta}{T_{at}} (P(r_1, t) - P(r_2, t)). \quad (6)$$

In Equation (6), the value of δ is 7.86×10^{-4} K/Pa and T_{at} represents the absolute temperature (unit: K), where $T_{at} = 273 + T$.

The relationship [25,26] between the density of a gas ρ (unit: kg/m^3) and the gas pressure P (unit: Pa) is shown in Equation (7).

$$\rho = \frac{PM}{RT_{at}}. \quad (7)$$

In Equation (7), R represents the molar gas constant, about 8.3145 $J \cdot K^{-1} \cdot mol^{-1}$ [26]; and M indicates the gas molar mass (unit: kg/mol).

Therefore, the difference in refractive indices at the positions of the two light beams in the MI, $n_1(t) - n_2(t)$, can be expressed as follows:

$$n_1(t) - n_2(t) = \frac{R\delta}{M} (\rho(r_1, t) - \rho(r_2, t)). \quad (8)$$

In Equation (8), $\rho(r_1, t)$ indicates the density of a gas at the position of the light beam 1 in the MI (unit: kg/m^3); $\rho(r_2, t)$ represents the density of such a gas at the position of the light beam 2 in the MI (unit: kg/m^3).

Thus, according to Equations (6) and (8), the phase of the MI-based MeoM can be determined, as shown in Equations (9) and (10).

$$\Phi_{MI\text{-based MeoM}}(t) = \Phi_{MI}(t) = \frac{4\pi L_{LB}}{\lambda} \left(\frac{\delta}{T_{at}} (P(r_1, t) - P(r_2, t))\right), \quad (9)$$

$$\Phi_{MI\text{-based MeoM}}(t) = \Phi_{MI}(t) = \frac{4\pi L_{LB}}{\lambda} \left(\frac{R\delta}{M} (\rho(r_1, t) - \rho(r_2, t))\right). \quad (10)$$

Therefore, the relationship between the output light intensity of MI-based MeoM $I_{MI\text{-based MeoM}}(P(r_1, t) - P(r_2, t))$ (unit: W/m^2) and the difference between the gas pressures at the positions of the two light beams $P(r_1, t) - P(r_2, t)$ is shown in Equation (11).

$$I_{MI\text{-based MeoM}}(P(r_1, t) - P(r_2, t)) = 2I_0 \left(1 + \cos\left(\frac{4\pi L_{LB}}{\lambda} \left(\frac{\delta}{T_{at}} (P(r_1, t) - P(r_2, t))\right)\right)\right). \quad (11)$$

The relationship between the output light intensity of MI-based MeoM $I_{MI\text{-based MeoM}}(\rho(r_1, t) - \rho(r_2, t))$ (unit: W/m^2) and the difference between the gas densities at the positions of the two light beams $\rho(r_1, t) - \rho(r_2, t)$ is shown in Equation (12).

$$I_{MI\text{-based MeoM}}(\rho(r_1, t) - \rho(r_2, t)) = 2I_0 \left(1 + \cos\left(\frac{4\pi L_{LB}}{\lambda} \left(\frac{R\delta}{M} (\rho(r_1, t) - \rho(r_2, t))\right)\right)\right). \quad (12)$$

It can be seen from Equations (11) and (12) that the difference in the gas pressures and densities at the positions of the two light beams in the MI results in a change in the output light intensity of MI-based MeoM (Schematic (3) in Figure 1a). The mathematical models have enabled gas concentration sensing based on the PA effect [27]. PA signals can be measured based on the PA effect by placing a PA gas cell on the two beam paths in the MI-based MeoM (Figure 1b). Figure 1b shows that the sensing system consists of a MeoM (a MI system) and a PA gas cell. A collimated light beam from a laser is propagated on a beam splitter through fiber port 1, and the incident light is split by the beam splitter into two parallel beams of equal intensity to pass through the PA gas cell. After the light beam is reflected by a reflector on the other side of the PA gas cell, it is recombined by the beam splitter and output to a photodetector through fiber port 2. On the side of the PA gas cell away from the two light beams, a light beam emitted by an excitation light source outside the PA gas cell is directed at a mirror. The gas in the PA gas cell generated sound waves (PA signals) with the same frequency as the excitation light output by the excitation light source due to the PA effect [24,27]. The design of the PA gas cell is based on the use of sound resonance [24]. According to Equations (11) and (12), the gas pressures and gas densities in the PA gas cell are different at the positions of the two light beams of the MeoM, resulting in a phase change of the interference light formed by the two reflected beams coming across the photodetector. This oscilloscope in Figure 1b can show its changes. Therefore, detecting different PA signals caused by different gas concentrations can be performed by measuring the phase or intensity change of the interference light, thereby detecting gas concentrations. This method offers a completely static measurement system (MI-based MeoM) and allows for the separation of the PA gas cell from the measurement system for application in harsh environments [24,27]. The gas-sensing method is called the MI-based MeoM–PAS method due to the combination of MI-based MeoM and PAS [24,27]. In addition, this method is also referred to as MI-based PAI because it combines the PA effect with an interferometer [24]. Our group used this gas-sensing method with a long-term stable and power-controlled fiber-coupled laser diode, while maintaining the length of the PA gas cell at 84 mm, the height at 14 mm, the width at 34 mm, the distance between the two light beams at 14 mm, the distance between the light beam nearest to the excitation source and the PA gas cell's wall closest to the other light beam at 28 mm, and the distance between the excitation source and the nearest light beam at 42 mm, to generate an excitation light with a power of 3500 mW and a modulation frequency of approximately 12.25 kHz, resulting in a PA signal with a frequency of about 12.25 kHz, thereby achieving a high sensitivity of gas concentration measurements with a low LOD [24,27]. Enhancing the excitation light power (e.g., more than 3500 mW) can increase the intensity of the PA signals [3,5]. However, the excitation light frequency and all the dimensional parameters of the PA gas cell are chosen to meet the conditions for the formation of standing sound waves and maximize the gas pressure difference at the positions of the two light beams [27]. In summary, our group's previous research has experimentally proven the workability of this gas-sensing method [24,27].

Similar to our group's previous research [24,27], aluminum, which is a common and frequently used material for manufacturing the PA gas cell [2–14], is a first choice as a material for the PA gas cell to conduct initial research quite easily and flexibly and later consider other materials. The density of aluminum is 2700 kg/m^3 at 1 atm and 20 °C [28], and the sound velocity in aluminum is 6420 m/s at 1 atm and 20 °C [29]. Additionally, the air density is 1.204 g/L at 1 atm and 20 °C [30], and the sound velocity in air is 343 m/s at 1 atm and 20 °C [31]. Because PA signals are sound signals in essence [1–3], the K-space pseudo-spectral method [32] (precision: res = 2) based on an identical sound source, which has the advantages of requiring fewer nodes, allowing larger time steps, easy coding, and high computational efficiency compared to the conventional finite element method (FEM) and boundary element method (BEM) [32,33], is utilized to investigate the dependence of this method on the fundamental parameters of a PA gas cell at the PA signal (sound wave) frequencies of approximately 12.25 kHz, 8.17 kHz, and 14.29 kHz by constructing

the above mathematical models, including the distance between the two light beams d, the PA gas cell's length L, the PA gas cell's height H, and the distance between the excitation source and the nearest light beam D (Figure 1c). These three frequencies are selected because the PA gas cell length is an integer multiple of the half wavelengths of these three PA signals. Furthermore, the cell length and design variations must maintain a sound resonance condition to ensure that the PA gas cell functions as a resonant cell [34]. Due to the shape of the PA gas cell in this paper being a cuboid, the cell length must be an integer multiple of half the wavelength of sound waves (PA signals), and any design variations must also be integer multiples of half the wavelength of sound waves [24,34]. In addition, the excitation light source needs to be placed at the peak or valley of the PA signals to maximize the pressures at the positions of the two light beams under equivalent conditions [24,27]. It's worth noting that the length of the PA gas cell L must be an integer multiple ξ of the half-wavelength of the PA signals $\frac{\lambda_{PA}}{2}$ to form the standing sound waves under the condition that the PA gas cell is resonant and the light beam nearest to the excitation source is always kept at a constant position of λ_{PA} from the PA gas cell's wall closest to the other light beam. Therefore, the distance between the excitation source and the nearest light beam can be calculated by the expression $D = \xi \frac{\lambda_{PA}}{2}$ ($1 \leq \xi \leq \left(\frac{2L}{\lambda_{PA}} - 3\right)$ and ξ is a positive integer) when the excitation source is at the position of the peak or valley of the PA signals.

3. Analyses and Discussions

3.1. Fundamental Parametric Dependence of a PA Gas Cell

Figure 2a–c shows the pressure results in the time domain at the positions of the two light beams for PA signal frequencies of approximately 12.25 kHz, 8.17 kHz, and 14.29 kHz, at a signal-to-noise ratio (SNR) of 10 dB, and their corresponding differences, where the SNR value provides a good influence on behavior; however, other values could also be selected. The distance of the two light beams (14 mm for approximately 12.25 kHz, 21 mm for about 8.17 kHz, and 12 mm for approximately 14.29 kHz), the PA gas cell's length (84 mm), the PA gas cell's height (14 mm), the distance between the light beam nearest to the excitation source and the PA gas cell's wall closest to the other light beam (28 mm for approximately 12.25 kHz, 42 mm for about 8.17 kHz, and 24 mm for approximately 14.29 kHz), and the distance of the excitation source from the nearest light beam (42 mm for approximately 12.25 kHz, 21 mm for about 8.17 kHz, and 36 mm for about 14.29 kHz) are kept constant. These dimensions, except for the height value, are chosen because they are integer multiples of the half-wavelength of the three corresponding PA signals, respectively. The frequency responses of their pressure differences are shown in Figure 2d–f, with values of 1.0155 Pa for approximately 12.25 kHz, 0.73205 Pa for about 8.17 kHz, and 1.1364 Pa for approximately 14.29 kHz, respectively.

The frequency responses are used to investigate the dependence of the MI-based MeoM–PAS gas-sensing method on the distance between the two light beams in the PA gas cell while keeping the PA gas cell's length (84 mm), the PA gas cell's height (14 mm), the distance between the light beam nearest to the excitation source and the PA gas cell's wall closest to the other light beam (28 mm for approximately 12.25 kHz, 42 mm for about 8.17 kHz, and 24 mm for about 14.29 kHz), and the distance of the excitation source from the nearest light beam (42 mm for approximately 12.25 kHz, 21 mm for about 8.17 kHz, and 36 mm for about 14.29 kHz) constant. In this method, the effect of the distance between the two light beams is investigated by changing the position of the light beam away from the excitation source. The PA gas cell used here is resonant, and the excitation source is located at the peak or valley position of the PA signals.

Figure 3a–c illustrates the relationship between the distance of the two light beams d (unit: mm) and the pressure difference P_1 (unit: Pa) at a PA signal frequency of approximately 12.25 kHz, 8.17 kHz, and 14.29 kHz, respectively:

$$P_1 = A \sin(\alpha d + B). \quad (13)$$

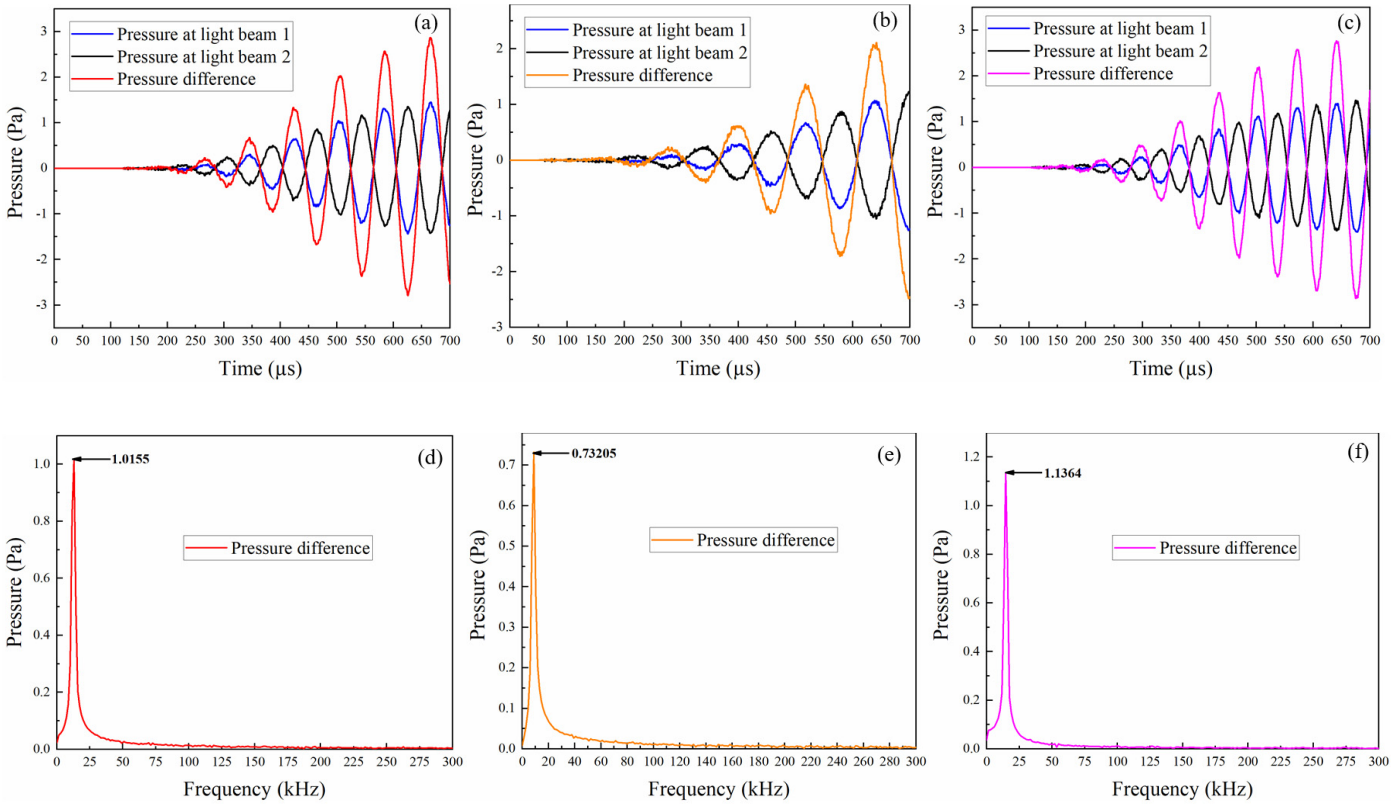

Figure 2. Pressure results in the time domain at the positions of the two light beams at (**a**) approximately 12.25 kHz, (**b**) about 8.17 kHz, and (**c**) approximately 14.29 kHz, and their difference. Frequency response of the pressure difference at (**d**) approximately 12.25 kHz, (**e**) about 8.17 kHz, and (**f**) approximately 14.29 kHz.

The relevant parameters and R^2 coefficients of Equation (13) at different PA signal frequencies are shown in Table 1.

Table 1. Relevant parameters and R^2 coefficients of Equation (13) at different PA signal frequencies.

Frequency (kHz)	A	α	B	R^2
12.25	0.9336	0.1242	−0.3379	0.968
8.17	0.6755	0.07871	−0.2187	0.9501
14.29	1.075	0.1501	−0.4309	0.9659

Figure 3a–c shows that the pressure difference is a sine function of the distance between the two light beams. This indicates that the phase of the MI-based MeoM–PAS gas-sensing method also follows a sine function of the distance between the two light beams in the PA gas cell, provided that the PA gas cell is a resonant cell and the excitation source is positioned at the peak or valley of the PA signals.

The frequency responses are used to investigate the dependence of the MI-based MeoM–PAS gas-sensing method on the length of the PA gas cell while keeping the distance between the two light beams (14 mm for approximately 12.25 kHz, 21 mm for about 8.17 kHz, and 12 mm for approximately 14.29 kHz), the PA gas cell's height (14 mm), the distance between the light beam nearest to the excitation source and the PA gas cell's wall closest to the other light beam (28 mm for approximately 12.25 kHz, 42 mm for about 8.17 kHz, and 24 mm for about 14.29 kHz), and the distance of the excitation source from the nearest light beam (42 mm for approximately 12.25 kHz, 21 mm for about 8.17 kHz, and 36 mm for approximately 14.29 kHz) constant. In this case, the length of the PA gas cell is adjusted in increments of half the wavelength of the PA signals to satisfy the requirement

that the PA gas cell function as a resonant cell. Furthermore, the excitation source is located at the peak or valley position of the PA signals.

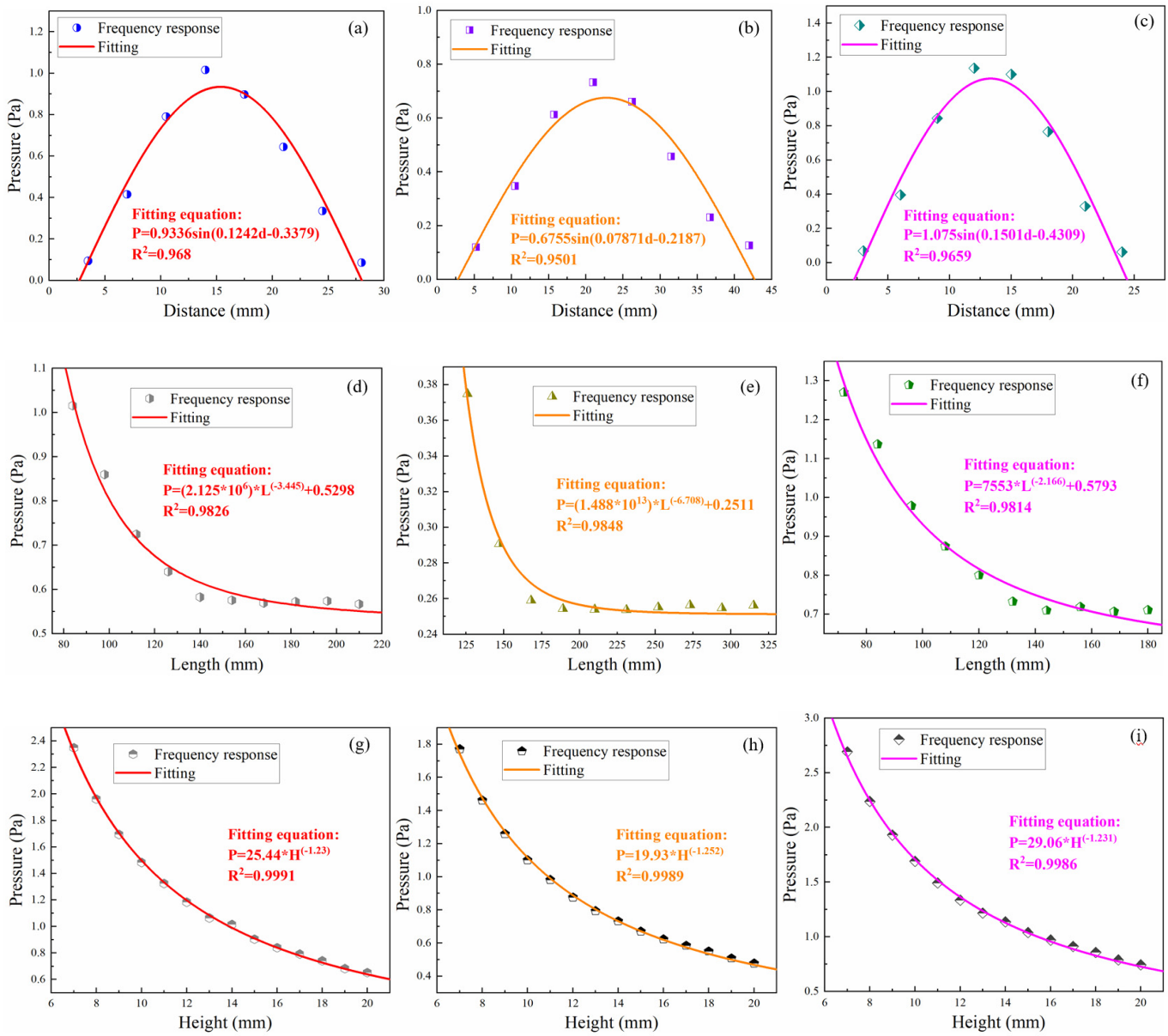

Figure 3. The relationship between the distance of the two light beams and the pressure difference at (**a**) approximately 12.25 kHz, (**b**) about 8.17 kHz, and (**c**) approximately 14.29 kHz. The relationship between the length of the PA gas cell and the pressure difference at (**d**) approximately 12.25 kHz, (**e**) about 8.17 kHz, and (**f**) approximately 14.29 kHz. The relationship between the height of the PA gas cell and the pressure difference at (**g**) approximately 12.25 kHz, (**h**) about 8.17 kHz, and (**i**) approximately 14.29 kHz.

Figure 3d–f shows the relationship between the length of the PA gas cell L (unit: mm) and the pressure difference P_2 (unit: Pa) at a PA signal frequency of about 12.25 kHz, 8.17 kHz, and 14.29 kHz, respectively:

$$P_2 = \eta L^{\beta} + C. \quad (14)$$

The relevant parameters and R^2 coefficients of Equation (14) at different PA signal frequencies are shown in Table 2.

Table 2. Relevant parameters and R^2 coefficients of Equation (14) at different PA signal frequencies.

Frequency (kHz)	η	β	C	R^2
12.25	2.125×10^6	−3.445	0.5298	0.9826
8.17	1.488×10^{13}	−6.708	0.2511	0.9848
14.29	7553	−2.166	0.5793	0.9814

Figure 3d–f demonstrates that the pressure difference follows a power exponent function of the cell length. This suggests that the phase of the MI-based MeoM–PAS gas-sensing method follows a power exponent function of the length of the PA gas cell, provided that the PA gas cell functions as a resonant cell and the excitation source is located at the peak or valley position of the PA signals.

The frequency responses are used to investigate the dependence of the MI-based MeoM–PAS gas-sensing method on the height of the PA gas cell while keeping the distance between the two light beams (14 mm for approximately 12.25 kHz, 21 mm for about 8.17 kHz, and 12 mm for approximately 14.29 kHz), the PA gas cell's length (84 mm), the distance between the light beam nearest to the excitation source and the PA gas cell's wall closest to the other light beam (28 mm for approximately 12.25 kHz, 42 mm for about 8.17 kHz, and 24 mm for about 14.29 kHz), and the distance of the excitation source from the nearest light beam (42 mm for approximately 12.25 kHz, 21 mm for about 8.17 kHz, and 36 mm for approximately 14.29 kHz) constant. The PA gas cell used here functions as a resonant cell, and the excitation source is positioned at the peak or valley of the PA signals.

Figure 3g–i shows the relationship between the height of the PA gas cell H (unit: mm) and the pressure difference P_3 (unit: Pa) at a PA signal frequency of approximately 12.25 kHz, 8.17 kHz, and 14.29 kHz, respectively:

$$P_3 = \mu H^{\varepsilon}. \quad (15)$$

The relevant parameters and R^2 coefficients of Equation (15) at different PA signal frequencies are shown in Table 3.

Table 3. Relevant parameters and R^2 coefficients of Equation (15) at different PA signal frequencies.

Frequency (kHz)	μ	ε	R^2
12.25	25.44	−1.23	0.9991
8.17	19.93	−1.252	0.9989
14.29	29.06	−1.231	0.9986

Figure 3g–i demonstrates that the pressure difference varies as a power exponent of the cell height. This suggests that the phase of the MI-based MeoM–PAS gas-sensing method also varies as a power exponent of the height of the PA gas cell, provided that the PA gas cell functions as a resonant cell and the excitation source is located at the peak or valley position of the PA signals.

The frequency responses are used to study the dependence of the MI-based MeoM–PAS gas-sensing method on the distance of the excitation source from the nearest light beam while keeping the distance between the two light beams (14 mm for approximately 12.25 kHz, 21 mm for about 8.17 kHz, and 12 mm for approximately 14.29 kHz), the PA gas cell's length (168 mm), the PA gas cell's height (14 mm), and the distance between the light beam nearest to the excitation source and the PA gas cell's wall closest to the other light beam (28 mm for approximately 12.25 kHz, 42 mm for about 8.17 kHz, and 24 mm for about 14.29 kHz) constant. In this case, the distance of the excitation source from the nearest light beam is adjusted in increments of half a wavelength of the PA signals to ensure that the excitation source is situated at the peak or valley position of the PA signals. Additionally, the PA gas cell employed here operates as a resonant cell.

Figure 4a–c shows the relationship between the distance of the excitation source from the nearest light beam D (unit: mm) and the pressure difference P_4 (unit: Pa) at a PA signal frequency of about 12.25 kHz, 8.17 kHz, and 14.29 kHz, respectively:

$$P_4 = \sigma D^{\tau} + E. \quad (16)$$

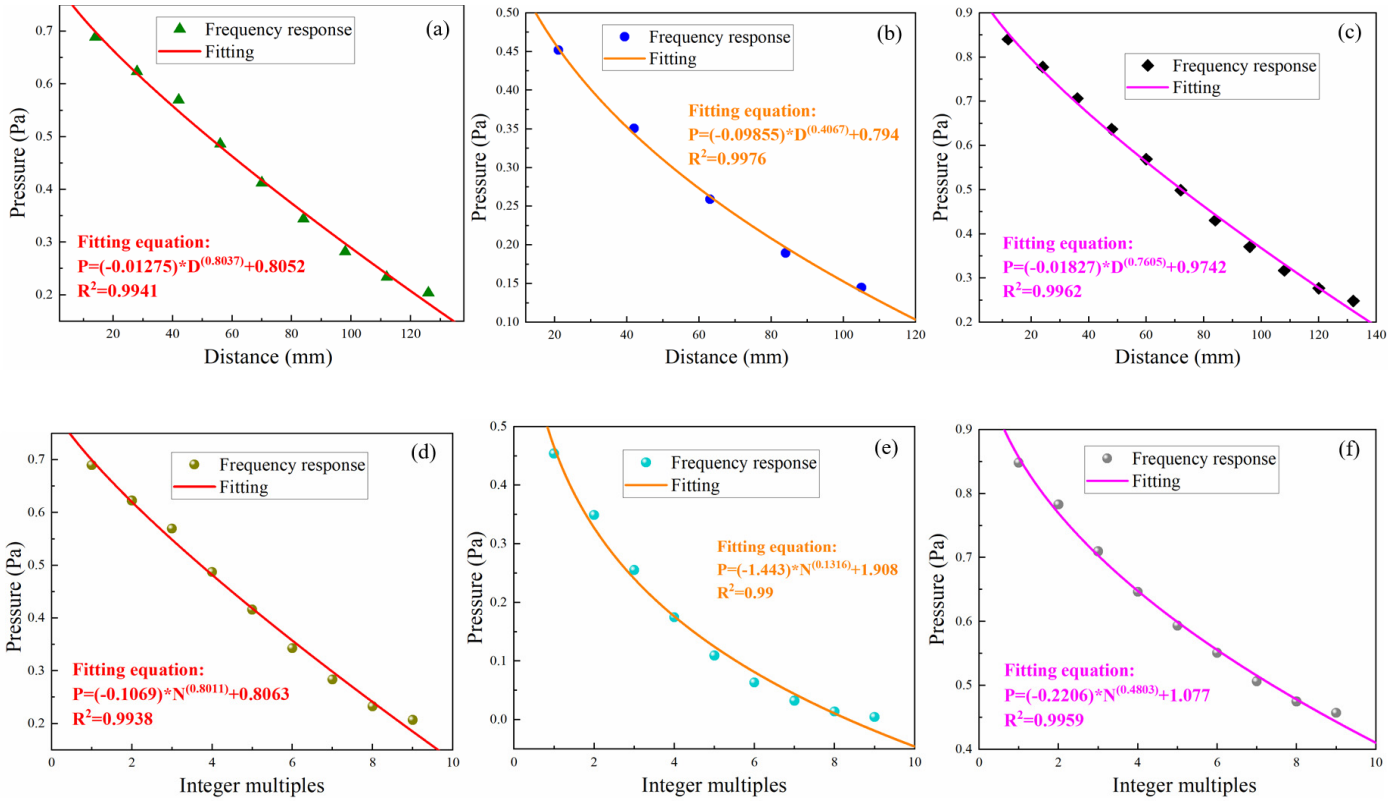

Figure 4. The relationship between the distance of the excitation source from the nearest light beam and the pressure difference at (**a**) approximately 12.25 kHz, (**b**) about 8.17 kHz, and (**c**) approximately 14.29 kHz. The relationship between the multiple of the distance of the excitation source from the nearest light beam and the half wavelength of the PA signals and the pressure difference at (**d**) approximately 12.25 kHz, (**e**) about 8.17 kHz, and (**f**) approximately 14.29 kHz.

The relevant parameters and R^2 coefficients of Equation (16) at different PA signal frequencies are shown in Table 4.

Table 4. Relevant parameters and R^2 coefficients of Equation (16) at different PA signal frequencies.

Frequency (kHz)	σ	τ	E	R^2
12.25	−0.01275	0.8037	0.8052	0.9941
8.17	−0.09855	0.4067	0.794	0.9976
14.29	−0.01827	0.7605	0.9742	0.9962

Figure 4a–c demonstrates that the pressure difference follows a power exponent function of the distance of the excitation source from the nearest light beam. This occurs when the length of the PA gas cell is identical at three different PA signal frequencies, provided that the PA gas cell functions as a resonant cell and the excitation source is positioned at the peak or valley of the PA signals.

The frequency responses are used to investigate the dependence of the MI-based MeoM–PAS gas-sensing method on the positive integer multiple, which is the multiple of the distance of the excitation source from the nearest light beam and the half wavelength of

the PA signals, while keeping the distance between the two light beams (14 mm for approximately 12.25 kHz, 21 mm for about 8.17 kHz, and 12 mm for approximately 14.29 kHz), the PA gas cell's length (168 mm for approximately 12.25 kHz, 252 mm for about 8.17 kHz, and 144 mm for approximately 14.29 kHz), the PA gas cell's height (14 mm), and the distance between the light beam nearest to the excitation source and the PA gas cell's wall closest to the other light beam (28 mm for approximately 12.25 kHz, 42 mm for about 8.17 kHz, and 24 mm for about 14.29 kHz) constant. The PA gas cell used here functions as a resonant cell.

Figure 4d–f illustrates the relationship between the positive integer multiple N, which is the multiple of the distance of the excitation source from the nearest light beam and the half wavelength of the PA signals, and the pressure difference P_5 (unit: Pa) at a PA signal frequency of approximately 12.25 kHz, 8.17 kHz, and 14.29 kHz, respectively:

$$P_5 = \kappa N^{\theta} + F. \quad (17)$$

The relevant parameters and R^2 coefficients of Equation (17) at different PA signal frequencies are shown in Table 5.

Table 5. Relevant parameters and R^2 coefficients of Equation (17) at different PA signal frequencies.

Frequency (kHz)	κ	θ	F	R^2
12.25	−0.1069	0.8011	0.8063	0.9938
8.17	−1.443	0.1316	1.908	0.99
14.29	−0.2206	0.4803	1.077	0.9959

Figure 4d–f shows that the pressure difference is a power exponent of the positive integer multiple, which corresponds to the multiple of the distance of the excitation source from the nearest light beam and the half wavelength of the PA signals. This occurs when the length of the PA gas cells differs at three distinct PA signal frequencies while the PA gas cell functions as a resonant cell.

Figure 4a–f indicates that the phase of the MI-based MeoM–PAS gas-sensing method follows a power exponent of the distance of the excitation source from the nearest light beam, given that the PA gas cell functions as a resonant cell and the excitation source is located at the peak or valley of the PA signals.

Figure 5a shows the frequency responses of the pressure differences between the two light beams at an SNR of 10 dB for PA signal frequencies of about 4.08 kHz, 6.125 kHz, 8.17 kHz, 10.21 kHz, 12.25 kHz, 14.29 kHz, 16.33 kHz, and 18.38 kHz, respectively, while maintaining the distance of the two light beams (14 mm), the PA gas cell's length (84 mm), the PA gas cell's height (14 mm), the distance between the light beam nearest to the excitation source and the PA gas cell's wall closest to the other light beam (28 mm), and the distance of the excitation source from the nearest light beam (42 mm) constant. Figure 5b illustrates their variation. These frequencies are selected because the PA gas cell length is an integer multiple of the half wavelengths of these PA signals. As shown in Figure 5b, the frequency response is maximal when the PA signal frequency is about 12.25 kHz, where half the wavelength of the PA signal is approximately equal to the distance between the two light beams. Moreover, Figure 3a shows the changes in pressure differences at a PA signal frequency of approximately 12.25 kHz while varying the distance between the two light beams. The pressure difference is highest when the distance between the two light beams is 14 mm (equivalent to half the wavelength of the PA signal). Hence, the phase of this MI-based MeoM–PAS gas-sensing method is at its maximum when the distance between the two light beams is roughly half the wavelength of the PA signal.

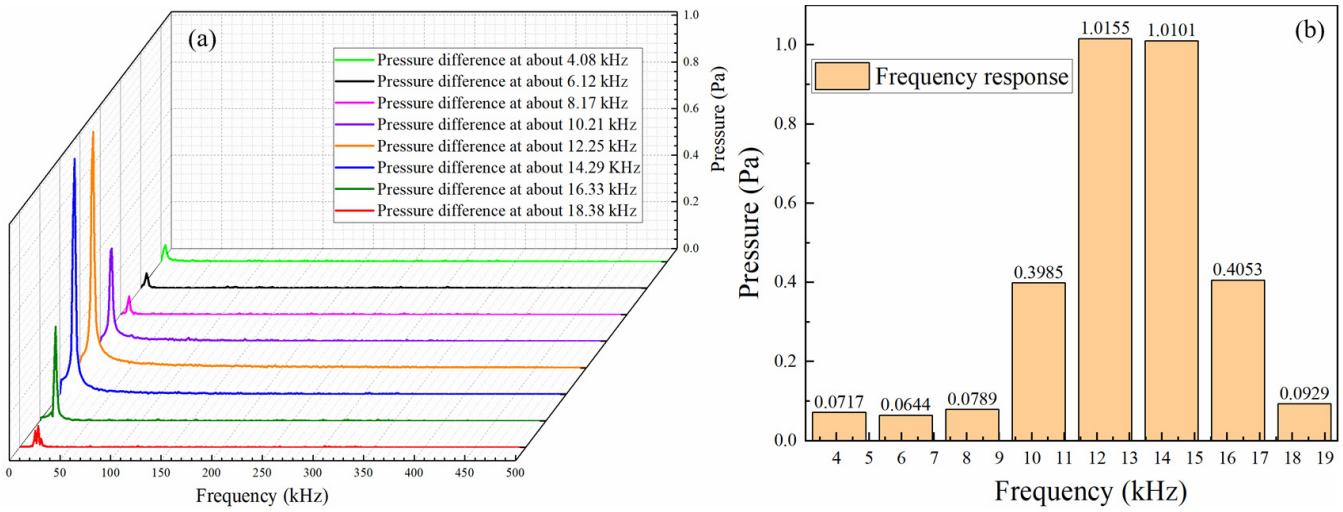

Figure 5. (**a**) Frequency responses of the pressure differences between the two light beams at an SNR of 10 dB for about 4.08 kHz, 6.125 kHz, 8.17 kHz, 10.21 kHz, 12.25 kHz, 14.29 kHz, 16.33 kHz, and 18.38 kHz, respectively. (**b**) The variation of the frequency responses for each frequency.

3.2. Dependence of a PA Gas Cell Using Non-Axial PA Signals

The PA gas cell dependence is investigated above by propagating PA signals vertically through the two light beams (axial PA signals). The dependence of a PA gas cell using non-axial PA signals is described in this section. The dimensions of the PA gas cell, including its length $L = 84\,mm$, width $W = 34\,mm$, and height $H = 14\,mm$, and the distance between the two light beams $d = 14\,mm$, as well as the distance between the light beam nearest to the excitation source and the PA gas cell's wall closest to the other light beam $2d = 28\,mm$, as well as the distance of the excitation source from the nearest light beam $D = 42\,mm$, remain unchanged as the PA signals propagate from perpendicular to the two light beams to propagating along the diagonal axis of the PA gas cell, as shown in Schematic (1) in Figure 6a. A comparison is then made between a 3D model of the PA signals propagating through a 3D gas cell (Schematic (2) in Figure 6a) and a 2D model of the PA signals propagating through a 2D plane along the diagonal axis (Schematic (3) in Figure 6a). The sound wave's frequency is approximately 11.36 kHz to meet the resonant cell condition [24,34]. The sound waves (PA signals) are fed directly into the 3D model along the diagonal axis (Schematic (4) in Figure 6a). As shown in Schematic (5) in Figure 6a, the sound waves (PA signals) are fed into the 2D model when the length is $\sqrt{W^2 + L^2} \approx 90.62\,mm$, the height is $H = 14\,mm$, the distance between the two light beams is $\frac{d}{L}\sqrt{W^2 + L^2} \approx 15.10\,mm$, and the distance between the light beam nearest to the excitation source and the PA gas cell's wall closest to the other light beam is $\frac{2d}{L}\sqrt{W^2 + L^2} \approx 30.20\,mm$, as well as the distance of the excitation source from the nearest light beam is $\frac{D}{L}\sqrt{W^2 + L^2} \approx 45.31\,mm$.

Figure 6b,c shows the pressure results in the time domain at the positions of the two light beams for the 3D and 2D models and their differences, respectively, with an SNR of 10 dB, where the SNR value provides a good influence on behavior; however, other values could also be selected. The frequency responses of the pressure differences (0.3902 Pa for the 3D model and 0.3942 Pa for the 2D model) are shown in Figure 6d,e, respectively. Therefore, the difference between the results of the 3D and 2D models is negligible, and the dependence of a PA gas cell using non-axial PA signals can be described using a 2D model. This is consistent with the dependence principle of axial PA signals on the PA gas cell, including the changing rules for the distance between the two light beams, the cell length, the cell height, and the distance between the excitation source and the nearest light beam.

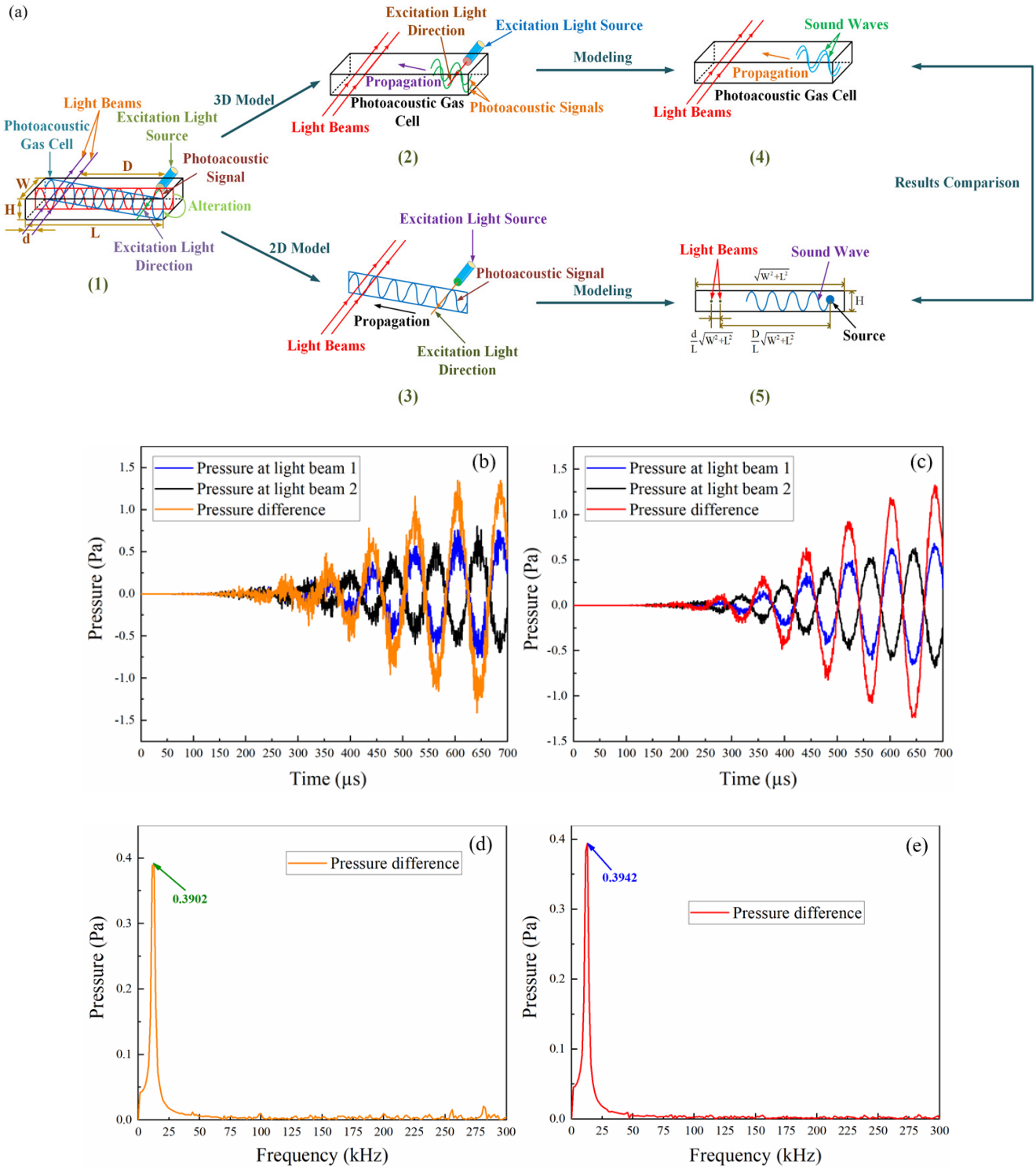

Figure 6. (**a**) Dependency exploration of a PA gas cell using non-axial PA signals: (1) the axial and non-axial PA signals in the 2D and 3D models; (2) the non-axial PA signals in the 3D model; (3) the non-axial PA signals in the 2D model; (4) the sound waves in the 3D model; and (5) the sound waves in the 2D model. Pressure results in the time domain at the positions of the two light beams and their differences for (**b**) the 3D model and (**c**) the 2D model at an SNR of 10 dB. Frequency responses of the pressure differences for (**d**) the 3D model and (**e**) the 2D model.

The pressure results for the 2D and 3D models are compared to further validate this conclusion by keeping the PA signals parallel to the two light beams. When the PA signals are parallel to the two light beams, the plane in which the signals are located is also parallel

to the two light beams. Thus, the pressure result for the 2D model should be 0 Pa. According to the above conclusion, the pressure result for the 3D model (Schematic (1) in Figure 7a) should also be 0 Pa when the sound waves (PA signals) are parallel to the two light beams (Schematic (2) in Figure 7a). Figure 7b shows the pressure results in the time domain at the positions of the two light beams for the 3D model, at an SNR of 10 dB, and their difference. The frequency responses of the pressure results at the positions of the two light beams for the 3D model (0.0417 Pa for light beam one and 0.0416 Pa for light beam two) are shown in Figure 7c. It can be seen from Figure 7b,c that the difference in pressure at the positions of the two light beams for the 3D models is approximately 0 Pa. Therefore, this confirms the validity of the conclusion presented in this section.

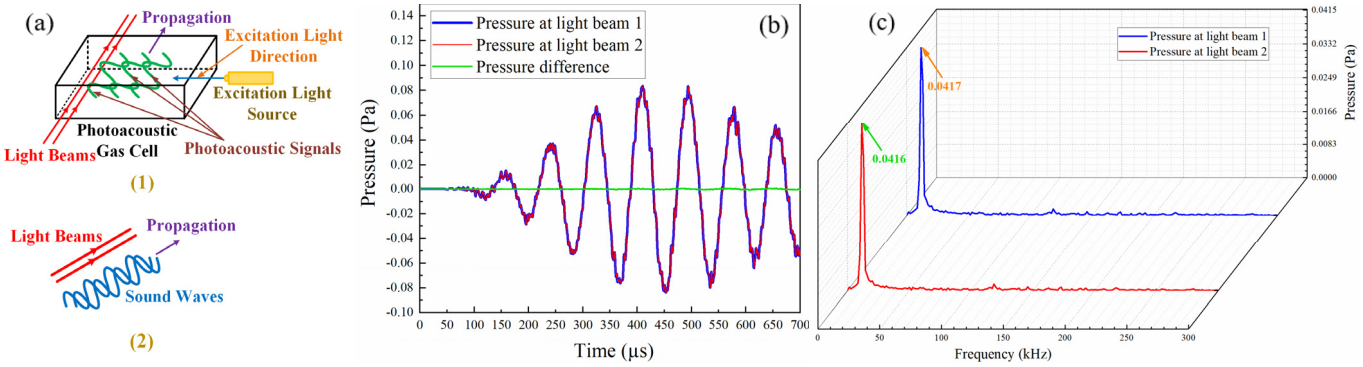

Figure 7. (**a**) The exploration in keeping the PA signals parallel to the two light beams in the 3D model: (1) the PA signals parallel to the two light beams; and (2) the sound waves parallel to the two light beams. (**b**) Pressure results in the time domain at the positions of the two light beams and their differences while keeping the PA signals parallel to the two light beams in the 3D model. (**c**) Frequency responses of the pressure results at the positions of the two light beams while keeping the PA signals parallel to the two light beams in the 3D model.

3.3. Selection of PA Gas Cell Materials

The relationship [35] between the absolute temperature T_{at} (unit: K) and the air density ρ (unit: kg/m^3) is shown in Equation (18).

$$\rho = \frac{pm}{k_B T_{at}}. \quad (18)$$

In Equation (18), p is the absolute pressure at 1 atm, around 101.325 × 10^3 Pa [35]; m shows the molecular mass of the dry air, approximately 4.81 × 10^{-26} kg [35]; and k_B represents the Boltzmann constant, about 1.380649 × 10^{-23} J · K^{-1} [35].

The relationship [36] between the sound velocity in the air c_s (unit: m/s) and the absolute temperature T_{at} (unit: K) is shown in Equation (19).

$$c_s = \sqrt{\gamma R_g T_{at}} \quad (19)$$

In Equation (19), γ represents the adiabatic index, generally given as 1.4 for air [36], and R_g is the gas constant, approximately 286.9 J · kg^{-1} · K^{-1} [36].

Equations (18) and (19) demonstrate that the fluctuations in temperature outside the PA gas cell can significantly affect the air density and propagation speed of PA signals inside the PA gas cell. This, in turn, may cause measurement errors due to the resulting fluctuations in the PA signals. Therefore, it is crucial to carefully select the material for the PA gas cell, with particular attention given to materials with low thermal conductivity that transmit heat slowly [37]. Using a low thermal conductivity material for the PA gas cell effectively resists the fluctuations in the temperature outside the PA gas cell.

In addition to aluminum, four additional common materials have been explored for producing the PA gas cell, which is often utilized as the material for constructing PA gas cells in the PAS research area. These materials include brass, glass, quartz, and stainless steel [2–14]. Table 6 shows the densities of these materials at 1 atm and 20 °C, while Table 7 indicates their sound velocities under the same conditions. We have also utilized the K-space pseudo-spectral method with a precision of 2 [32,33] to further discuss the selection of PA gas cell materials.

Table 6. Densities of four materials at 1 atm and 20 °C.

Material	Density (kg/m^3)	Ref.
Brass	8600	[28]
Glass	2320	[28]
Quartz	2650	[38]
Stainless steel	7740	[39]

Table 7. Sound velocities of four materials at 1 atm and 20 °C.

Material	Sound Velocity (m/s)	Ref.
Brass	4700	[29]
Glass	5640	[29]
Quartz	5570	[40]
Stainless steel	5790	[29]

It is assumed that the aluminum-produced PA gas cell is affected by a drastic change in the external temperature, which fluctuates between 0 and 100 °C in steps of 10 °C. Table 8 shows the thermal conductivities of the five materials considered, with aluminum having the highest thermal conductivity (237 $W/(m \cdot K)$) among them. It is used as a benchmark, and no delay is assumed in the temperature change of the aluminum-produced PA gas cell. On a 20 °C basis, the temperature outside the PA gas cell changes from 20 to 100 °C and from 20 to 0 °C in steps of 10 °C, and the temperature inside the PA gas cell changes accordingly. Air densities and sound velocities in air at 0, 10, 20, 30, 40, 50, 60, 70, 80, 90, and 100 °C, which are converted to the corresponding absolute temperature values, are then calculated using Equations (18) and (19). These values are used to determine the pressure results of the aluminum-produced PA gas cell at the positions of the two light beams. Figure 8a–c illustrates the frequency responses of the differences in pressure results of the aluminum-produced PA gas cell at the positions of the two light beams when SNR = 5 dB, 8 dB, and 10 dB, respectively. These SNR values provide a good impact on behavior; however, other values could also be chosen. The PA signal frequency is 12.25 kHz, the distance between the two light beams is 14 mm, the PA gas cell's length is 84 mm, the PA gas cell's height is 14 mm, the distance between the light beam nearest to the excitation source and the PA gas cell's wall closest to the other light beam is 28 mm, and the distance of the excitation source from the nearest light beam is 42 mm. The relationship between the frequency responses of the aluminum-produced PA gas cell and the temperature outside the PA gas cell is shown in Figure 8d.

Table 8. Thermal conductivities of five materials.

Material	Thermal Conductivity (W/(m·K))	Ref.
Aluminum	237	[41]
Brass	146.87	[42]
Glass	1.143	[43]
Quartz	3	[38]
Stainless steel	15.03	[42]

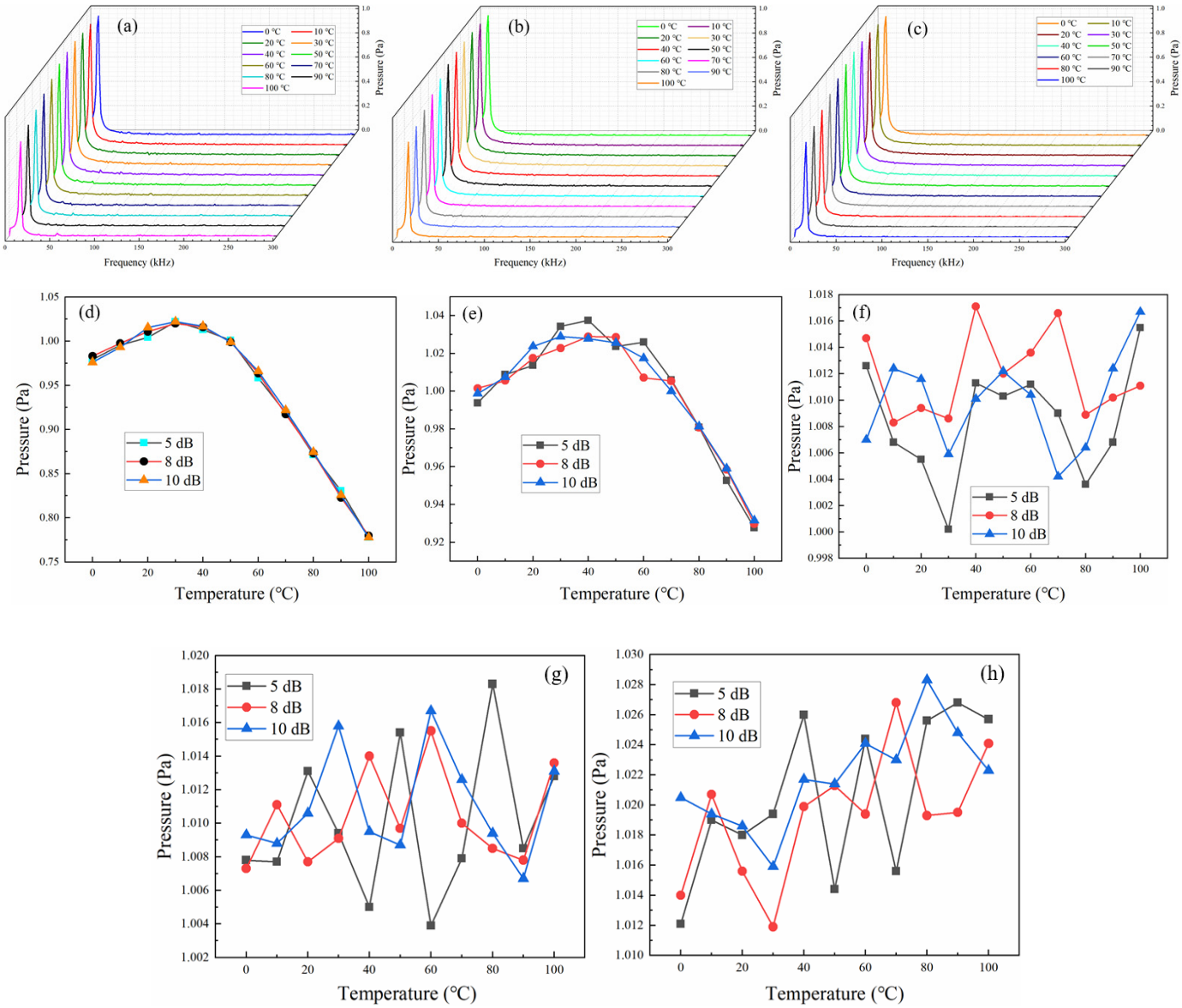

Figure 8. Frequency response of the difference in the pressure results at the positions of the two light beams in the aluminum-produced PA gas cell at (**a**) SNR = 5 dB, (**b**) SNR = 8 dB, and (**c**) SNR = 10 dB. The relationship between the frequency response of (**d**) the aluminum-produced PA gas cell, (**e**) the brass-produced PA gas cell, (**f**) the glass-produced PA gas cell, (**g**) the quartz-produced PA gas cell, and (**h**) the stainless steel-produced PA gas cell and the external temperature.

It is assumed that the walls of the PA gas cells produced by five different materials have the same thickness, and the initial internal and external temperatures of the PA gas cells produced by five materials is 20 °C. The external temperature of the aluminum-produced PA gas cell changes from 20 °C to φ, which means that the internal temperature of the PA gas cell also changes from 20 °C to φ, and the temperature difference is $\Delta T_{aluminum} = |20 - \varphi|$ (unit: °C). Then the same external temperature variation is configured for the PA gas cells produced by other materials, and the temperature variation inside the PA gas cells produced by other materials $\Delta T_{other\ materials}$ (unit: °C) can be calculated by Equation (20).

$$\Delta T_{other\ materials} = \frac{k_{other\ materials}}{k_{aluminum}} \Delta T_{aluminum}. \quad (20)$$

In Equation (20), $k_{other\ materials}$ represents the thermal conductivities of other materials (unit: $W/(m \cdot K)$); and $k_{aluminum}$ is the thermal conductivity of the aluminum material (unit: $W/(m \cdot K)$).

According to Equation (20), the internal temperature of the PA gas cells, manufactured by brass, glass, quartz, and stainless steel, respectively, can be obtained by changing the external temperature from 20 to 100 °C and from 20 to 0 °C. They are converted to the corresponding absolute temperature values and then substituted into Equations (18) and (19) to obtain the air density and sound velocity of air values at different temperatures. Therefore, the frequency responses of the differences in the pressure results at the positions of the two light beams in the PA gas cells produced by brass, glass, quartz, and stainless steel, respectively, can be obtained by using these values and the K-space pseudo-spectral method [32,33] at SNR = 5 dB, 8 dB, and 10 dB, when the external temperature is varied. These results are shown in Figure 8e–h, assuming a distance of 14 mm between the two light beams, a PA gas cell length of 84 mm, a PA gas cell height of 14 mm, a distance of 28 mm between the light beam nearest to the excitation source and the PA gas cell's wall closest to the other light beam, a distance of 42 mm between the excitation source and the nearest light beam, and a PA signal frequency of 12.25 kHz.

Figure 9a–e illustrates the differences between the maximum and minimum values of five tests for the frequency responses of the PA gas cells that are produced by aluminum, brass, glass, quartz, and stainless steel, respectively, at an SNR of 5 dB, 8 dB, and 10 dB. Figure 9f shows the mean values of these tests at an SNR of 5 dB, 8 dB, and 10 dB, respectively.

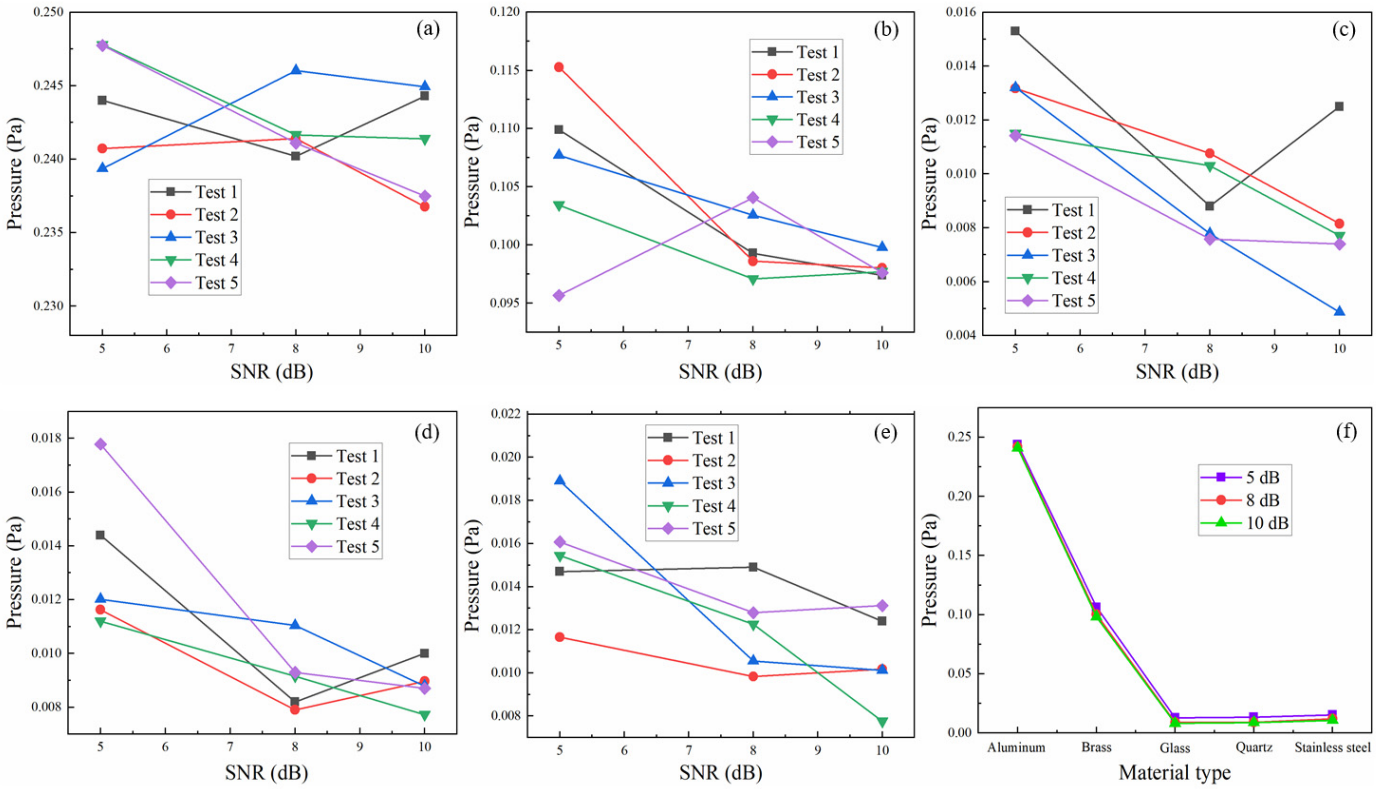

Figure 9. The differences between the maximum and minimum values of five tests for the frequency responses of (**a**) the aluminum-produced PA gas cell, (**b**) the brass-produced PA gas cell, (**c**) the glass-produced PA gas cell, (**d**) the quartz-produced PA gas cell, and (**e**) the stainless steel-produced PA gas cell, at SNR = 5 dB, 8 dB, and 10 dB. (**f**) Mean values of five test differences for the PA gas cells produced by five common materials under the influence of external temperatures.

Figure 9f indicates that the glass-produced PA gas cell demonstrates the best performance against fluctuations in external temperature. However, the quartz- and stainless steel-produced gas cells have exhibited similar resistance to these changes.

Choosing suitable materials for a PA gas cell can appropriately prevent noise influence [44]. The sound absorption coefficient (SAC) is typically used to describe the sound absorption performance of a material [44,45]. SAC is the ratio between the sum of the absorbed and transmitted sound energy of a material and the input sound energy [45], and its value ranges from 0 to 1 [44]. When SAC = 0, the material cannot absorb sound energy, any sound energy input to the material can be reflected [44,45]. When SAC = 1, the material fully absorbs and transmits all input sound energy, meaning that any sound energy input to the material cannot be reflected [44,45]. The higher the SAC value of a material, the better its ability to absorb and transmit sound energy [44]. However, SAC is frequency-dependent [44,45], making it inconvenient for quantitative assessment. Therefore, the noise reduction coefficient (NRC), an average absorption coefficient, is generally used to assess the sound absorption performance of a material [46].

The NRC is the average of the SAC values at 250 Hz, 500 Hz, 1000 Hz, and 2000 Hz [46,47]. A lower NRC value indicates a stronger ability of the material to reflect sound energy [47]. Table 9 shows the NRC values of five common materials—aluminum, brass, glass, quartz, and stainless steel—considered for the PA gas cell, and it is used to discuss the selection of these five materials while keeping the same thickness of the PA gas cells' walls. Table 9 indicates that glass has the lowest NRC value (0.15) and aluminum has the highest NRC value (0.53) of the five materials. Therefore, if the goal is to resist the noise influence outside the PA gas cell, the material used to manufacture the gas cell should be glass, but if the goal is to decrease the noise influence inside the PA gas cell, the material used to manufacture the gas cell should be aluminum. Figure 9f shows that aluminum is less resistant to temperature fluctuations outside the PA gas cell than the other four materials. In addition, materials with an NRC value of less than 0.2 are generally considered sound-reflecting materials, and those with an NRC greater than or equal to 0.2 are considered sound-absorbing materials [46,47]. It can be seen from Table 9 that glass is the only one of the five materials with an NRC value of less than 0.2 and is therefore not conducive to reducing the noise influence inside the PA gas cell. Neither aluminum nor glass is the best option for the PA gas cell. Figure 9f shows that quartz and stainless steel, in addition to glass, also exhibit great performance in resisting the fluctuations in temperature outside the PA gas cell. Furthermore, Table 9 shows that the NRC values for both quartz and stainless steel are greater than 0.2, indicating that they can help to reduce the noise influence inside the PA gas cell. In addition, both quartz and stainless steel have much smaller NRC values than the initial material, aluminum, so they are more resistant to the influence of external noise from the PA gas cell than aluminum.

Table 9. Noise reduction coefficients (NRC) of five materials.

Material	Noise Reduction Coefficient (NRC)	Ref.
Aluminum	0.53 (median of 0.44–0.62 in Ref. [48])	[48]
Brass	0.25 (NRC calculated by SAC in Ref. [49])	[49]
Glass	0.15 (median of 0.1–0.2 in Ref. [50])	[50]
Quartz	0.35 (mean of 0.21, 0.33, 0.37, 0.42, and 0.44 in Ref. [51])	[51]
Stainless steel	0.23 (mean of 0.34, 0.25, 0.19, and 0.15 in Ref. [52])	[52]

Therefore, considering both resistance to temperature fluctuations outside the PA gas cell and the influence of noise inside and outside the PA gas cell, the PA gas cells produced with quartz and stainless steel are the better options.

It is not sufficient to select the materials used to manufacture the PA gas cell to reduce the noise influence inside or outside the PA gas cell [3,53]. To reduce the influence of external noise, the PA gas cell should have good airtightness and a relatively wide wall thickness in addition to the selection of the manufacturing materials, and the resonant

frequency of the PA gas cell should not be below 1000 Hz [1,53]. The noise influence of the gas flow inside the PA gas cell can be reduced by controlling the gas flow, modifying the PA gas cell shape, and optimizing the PA gas cell design and manufacturing techniques [54]. The electrical noise is generally non-coherent, and its influence can be reduced by phase-sensitive detection techniques [53]. In addition, the PA gas sensing system should be considered for an electromagnetic shielding design to prevent mutual interference between external electromagnetic interference and internal electromagnetism in the system [2,53]. For a resonant PA gas cell, the effect of Brownian motion noise, which is noise caused by Brownian motion, can be reduced by causing the PA signal to form a standing wave [53,54]. In addition, the background signal noise is a coherent noise generated by the solid PA effect of the modulated light on the window glass and inner wall of the PA gas cell [53]. The noise cannot be reduced by phase-sensitive detection techniques [54]. If only the reduction of the background signal noise influence is considered, the materials used to manufacture the PA gas cell should be those with a high thermal conductivity [53,54]. Aluminum is the best option based on the five common materials considered in this article (Table 8). However, according to the above research results, the ability of the PA gas cell to resist external temperature fluctuations is not optimized if aluminum continues to be used as the material for manufacturing the PA gas cell. In fact, in addition to the material selection of the PA gas cell, some other methods can also reduce the background signal noise influence, such as keeping the window glass of the PA gas cell clean and contamination-free, making the inner wall of the PA gas cell smooth enough, avoiding the contact of the light source with the inner wall of the PA gas cell, and keeping the diameter of the inlet hole of the PA gas cell large enough [53,54]. Therefore, the materials used to manufacture the PA gas cell are not the only factor determining the background signal noise influence. Therefore, considering these factors, quartz and stainless steel are still the better options for manufacturing the PA gas cell. Finally, reducing acoustic noise caused by the transmission of sound waves inside the PA gas cell also needs to be considered, which can be achieved by installing buffer chambers on the PA gas cell [53].

Thermal and viscous losses are also two key parameters in the selection of materials for manufacturing the PA gas cell [55]. Materials with high thermal conductivity and specific heat capacity should be considered to reduce thermal losses in the PA gas cell [53,55]. Therefore, aluminum should be used to produce the PA gas cell because it has the highest thermal conductivity ($237\,W/(m \cdot K)$) and specific heat capacity ($0.22\,cal/g \cdot {}^{\circ}C$), as shown in Tables 8 and 10. However, the aluminum-produced PA gas cell is less resistant to drastic changes in external temperature when it is used in a practical environment. Therefore, aluminum is probably not the best option for manufacturing the PA gas cell. Glass has the lowest thermal conductivity ($1.143\,W/(m \cdot K)$), and its specific heat capacity ($0.16\,cal/g \cdot {}^{\circ}C$) is not the highest of the five materials, as shown in Tables 8 and 10. Moreover, the glass-produced PA gas cell has a weak absorption effect on the noise inside the gas cell. Therefore, perhaps glass is not an ideal option for producing the PA gas cell either. The thermal conductivity of quartz ($3\,W/(m \cdot K)$) and stainless steel ($15.03\,W/(m \cdot K)$) is greater than that of glass, and stainless steel is better in comparison between them, but the specific heat capacity of quartz ($0.174\,cal/g \cdot {}^{\circ}C$) is greater than that of stainless steel ($0.117\,cal/g \cdot {}^{\circ}C$). In addition, viscous losses can be reduced by polishing and gold-plating the inner walls of the PA gas cell [54,55]. So, the selection of these five materials is mainly determined by the reduction of thermal losses. Therefore, considering the reduction in thermal and viscous losses, quartz and stainless steel are still the better options among the five common materials.

Table 10. Specific heat capacities of five materials.

Material	Specific Heat Capacity (cal/g · °C)	Ref.
Aluminum	0.22	[55]
Brass	0.092	[55]
Glass	0.16	[55]
Quartz	0.174	[56]
Stainless steel	0.117	[55]

In summary, this section discusses the selection of five common materials for the PA gas cell—aluminum, brass, glass, quartz, and stainless steel—under the influence of temperature fluctuations outside the PA gas cell and noise inside and outside the PA gas cell, as well as thermal and viscous losses inside the PA gas cell. Considering these factors, it can be concluded that the PA gas cells produced with quartz and stainless steel are the better options. In addition, a temperature and humidity compensation system could be attached to the interior of the PA gas cell to counteract the influence of temperature fluctuations and humidity variations inside the PA gas cell [57,58].

3.4. Sensitivity Enhancement

According to Equation (11), the sensitivity $|S(\Delta P(t))| = |S(P(r_1, t) - P(r_2, t))|$ (unit: $W \cdot m^{-2} \cdot Pa^{-1}$) of the MI-based MeoM–PAS gas-sensing method can be expressed as Equation (21).

$$|S(\Delta P(t))| = \left| \frac{dI_{\text{MI-based MeoM}}(\Delta P(t))}{d\Delta P(t)} \right| = \left| -\frac{8I_0\pi L_{LB}\delta}{\lambda T_{at}} \sin\left(\frac{4\pi L_{LB}\delta}{\lambda T_{at}} \Delta P(t)\right) \right|. \quad (21)$$

According to Equation (12), the sensitivity $|S(\Delta\rho(t))| = |S(\rho(r_1, t) - \rho(r_2, t))|$ (unit: $W \cdot m \cdot kg^{-1}$) of the gas-sensing method can be expressed in Equation (22).

$$|S(\Delta\rho(t))| = \left| \frac{dI_{\text{MI-based MeoM}}(\Delta\rho(t))}{d\Delta\rho(t)} \right| = \left| -\frac{8I_0\pi L_{LB}R\delta}{\lambda M} \sin\left(\frac{4\pi L_{LB}R\delta}{\lambda M} \Delta\rho(t)\right) \right|. \quad (22)$$

The relationship [59] between the light wavelength λ (unit: m) and the light frequency f (unit: Hz) is shown in Equation (23).

$$\lambda = \frac{c_L}{n_0 f}. \quad (23)$$

In Equation (23), c_L represents the light velocity in the air (unit: m/s); and n_0 represents the refractive index of the air, generally considered to be 1.0 [60].

Thus, Equations (21) and (22) can be transformed into Equations (24) and (25) according to Equation (23).

$$|S(\Delta P(t))| = \left| -\frac{8I_0\pi L_{LB}\delta f}{c_L T_{at}} \sin\left(\frac{4\pi L_{LB}\delta f}{c_L T_{at}} \Delta P(t)\right) \right|. \quad (24)$$

$$|S(\Delta\rho(t))| = \left| -\frac{8I_0\pi L_{LB}R\delta f}{c_L M} \sin\left(\frac{4\pi L_{LB}R\delta f}{c_L M} \Delta\rho(t)\right) \right|. \quad (25)$$

Equations (24) and (25) show that the sensitivity of the MI-based MeoM–PAS gas-sensing method is related to the length of the two light beams in the MI L_{LB}, the frequency of the incident light in the MI f, the intensity of the two light beams in the MI I_0, the gas molar mass M, the absolute temperature T_{at}, and the pressure difference $\Delta P(t)$ or gas density difference $\Delta\rho(t)$ between the positions of the two beams. Therefore, the sensitivity enhancement of this method is not fully determined by the pressure difference $\Delta P(t)$ or

gas density difference $\Delta\rho(t)$ between the positions of the two light beams. They can only guarantee the lower limit of the method's sensitivity.

Theoretically, when only the dimensions of the PA gas cell are changed in the whole sensing system, the pressure difference between the positions of the two light beams for a PA gas cell with a fixed size at a specific PA signal frequency is ΔP_1. According to the regulations presented in this article, the pressure difference between the positions of the two light beams for a PA gas cell with a smaller size at the same PA signal frequency is $n\Delta P_1$ (n is a multiple). Then, by deriving Equation (11), the sensitivity of the sensing system with a smaller gas cell is n times greater than that of the sensing system with a larger gas cell. Figure 10a,b show the pressure results in the time domain at the positions of the two light beams for PA signal frequencies of approximately 12.25 kHz and 14.29 kHz, at an SNR of 10 dB, and their corresponding differences. The distance of the two light beams (14 mm for approximately 12.25 kHz and 12 mm for approximately 14.29 kHz) is kept at one-half of the PA signal wavelength, the PA gas cell's length (56 mm for approximately 12.25 kHz and 48 mm for approximately 14.29 kHz) is kept at 4 times the half wavelength of the PA signal, the PA gas cell's height is kept at 14 mm, the distance between the light beam nearest to the excitation source and the PA gas cell's wall closest to the other light beam (28 mm for approximately 12.25 kHz and 24 mm for approximately 14.29 kHz) is kept at 1 times the wavelength of the PA signal, and the distance of the excitation source from the nearest light beam (14 mm for approximately 12.25 kHz and 12 mm for about 14.29 kHz) is kept at one-half of the PA signal wavelength. The frequency responses of their pressure differences are shown in Figure 10c,d, with values of 1.5318 Pa for approximately 12.25 kHz and 1.8402 Pa for approximately 14.29 kHz, respectively.

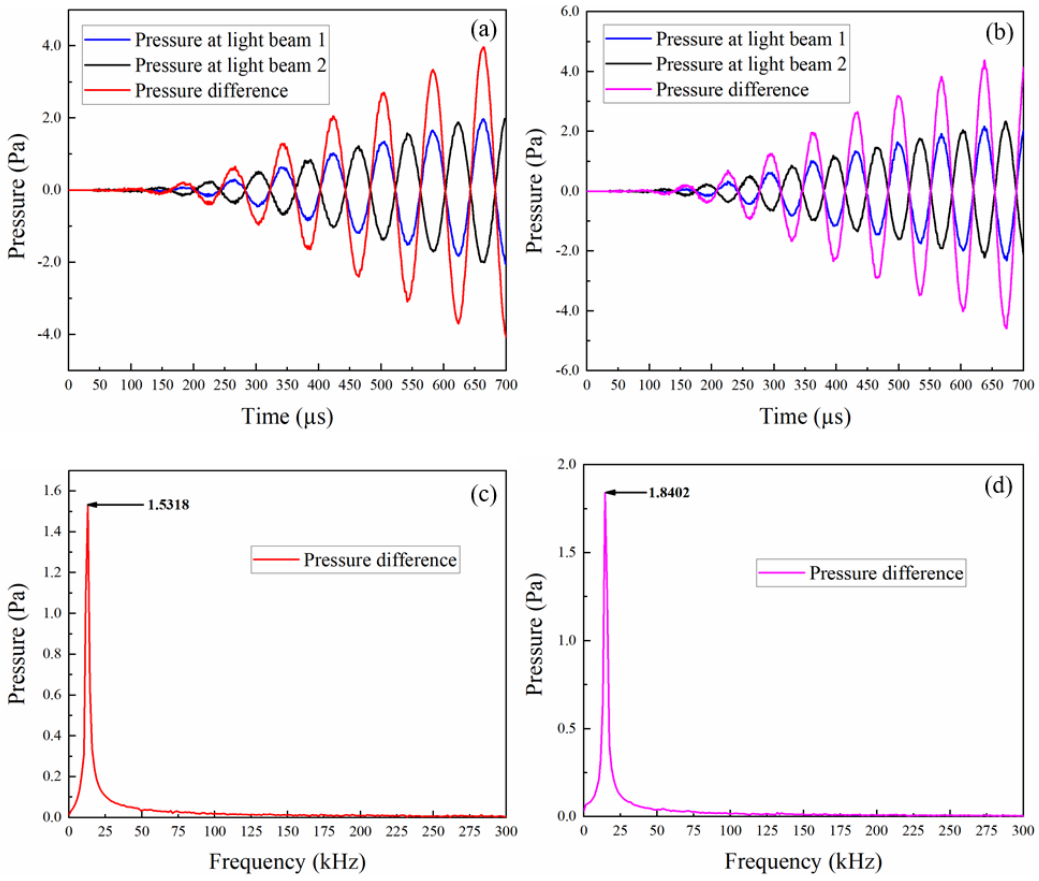

Figure 10. Pressure results in the time domain at the positions of the two light beams, at (**a**) approximately 12.25 kHz and (**b**) about 14.29 kHz, and their differences. Frequency responses of the pressure differences at (**c**) approximately 12.25 kHz and (**d**) about 14.29 kHz.

Figures 2d and 10c demonstrate that reducing the length of the PA gas cell from 84 mm to 56 mm and decreasing the distance between the excitation source and the nearest light beam from 42 mm to 14 mm, for a PA signal frequency of about 12.25 kHz, results in a pressure difference between the two light beams that is approximately 1.51 times greater. Similarly, Figures 2f and 10d indicate that reducing the length of the PA gas cell from 84 mm to 48 mm and decreasing the distance between the excitation source and the nearest light beam from 36 mm to 12 mm, for a PA signal frequency of approximately 14.29 kHz, results in a pressure difference between the two light beams that is approximately 1.62 times greater.

The derivation of Equation (11) shows that changing the dimensions of the PA gas cell alone can only marginally increase the method's sensitivity. However, in experiments, changing the dimensions of the PA gas cell can lead to a significant increase in sensitivity, which can reach tens or hundreds of times greater than the theoretical increase predicted by Equation (11) [61,62]. This is because the PA gas cell can only determine the lower sensitivity limit for this gas-sensing method [53,54]. In addition, if the width of the PA gas cell is also reduced, e.g., from 34 mm to 20 mm, the volume of the PA gas cell will also be smaller (from 39,984 mm^3 to 15,680 mm^3 for approximately 12.25 kHz and from 39,984 mm^3 to 13,440 mm^3 for about 14.29 kHz). Because the PA cell constant of the PA gas cell, which describes the ability of the gas in a PA cell to absorb light energy and convert it into sound waves, is inversely proportional to the volume of the PA gas cell, a new PA gas cell with a smaller volume, compared to the original PA gas cell, can lead to a stronger PA signal [54,63]. This can also lead to an increase in the method's sensitivity. In addition, many factors in experiments cannot be simulated, such as the interaction degree between the excitation light and the detected gas, etc. [53,54]. Therefore, it is not unexpected that the increase in sensitivity by tens or hundreds of times can be achieved by reducing the dimensions of a PA gas cell in the experiment [3,54]. Therefore, the arithmetic results presented in this article can only serve as a guide. When the dimensions of the PA gas cell are reduced, the actual enhancement in sensitivity of this method can only be obtained by experimentation.

4. Conclusions

In conclusion, this paper illustrates a mathematical model of the MI-based MeoM–PAS method, which is also referred to as MI-based PAI, for gas-sensing applications in complex and adverse environments because this method offers a completely static measurement system and separates the PA gas cell from the measuring system. This article also investigates the dependence of this method on the fundamental parameters of a cubical PA gas cell using axial PA signals. The results indicate that the phase of the method is a sine function of the distance between the two light beams and a power exponent of the PA gas cell's length, the PA gas cell's height, and the distance between the excitation source and the nearest light beam, under the condition that the PA gas cell is resonant and that the excitation source is at the position of the peak or valley of the PA signals. Additionally, the phase of the method is maximal when the distance between the two light beams is approximately half the wavelength of the PA signals under the same conditions that the PA gas cell is resonant and that the excitation source is at the position of the peak or valley of the PA signals. The dependence of a PA gas cell using non-axial PA signals is described under the condition that the PA gas cell is resonant, which follows the PA gas cell dependence principle of axial PA signals. This is consistent with the changing aforementioned parameters for the distance between the two light beams, the PA gas cell's length, the PA gas cell's height, and the distance between the excitation source and the nearest light beam. Furthermore, the selection of five common materials for the PA gas cell (aluminum, brass, glass, quartz, and stainless steel) is discussed under the influence of temperature fluctuations outside the PA gas cell, noise inside and outside the PA gas cell, as well as thermal and viscous losses inside the PA gas cell. The results indicate that quartz and stainless steel are promising options. Finally, the parameters related to the sensitivity enhancement of the gas-sensing method are analyzed

using mathematical models. The results demonstrate that reducing the dimensions of the PA gas cell can theoretically enhance the sensitivity of the gas-sensing method.

Author Contributions: Conceptualization, S.W.; methodology, S.W.; software, S.W.; validation, S.W.; formal analysis, S.W.; investigation, S.W.; resources, S.W.; data curation, S.W.; writing—original draft preparation, S.W.; writing—review and editing, A.K.Y., K.W., M.J. and A.W.K.; supervision, M.J. and A.W.K. All authors have read and agreed to the published version of the manuscript.

Funding: This work was supported by the China Scholarship Council (CSC) (Grant Nos. 202106050036 (Shuchao Wang) and 201808340074 (Kun Wang)) and the Technical University of Munich (TUM) in the framework of the Open Access Publishing Program.

Institutional Review Board Statement: Not applicable.

Informed Consent Statement: Not applicable.

Data Availability Statement: Data are available from S.W.

Conflicts of Interest: The authors declare no conflict of interest.

References

1. Hodgkinson, J.; Tatam, R.P. Optical Gas Sensing: A Review. *Meas. Sci. Technol.* **2013**, *24*, 012004. [CrossRef]
2. Yang, T.H.; Chen, W.G.; Wang, P.Y. A Review of All-Optical Photoacoustic Spectroscopy as a Gas Sensing Method. *Appl. Spectrosc. Rev.* **2021**, *56*, 143–170. [CrossRef]
3. Fathy, A.; Sabry, Y.M.; Hunter, I.W.; Khalil, D.; Bourouina, T. Direct Absorption and Photoacoustic Spectroscopy for Gas Sensing and Analysis: A Critical Review. *Laser Photonics Rev.* **2022**, *16*, 2100556. [CrossRef]
4. Wu, H.P.; Zhang, D.D.; Dong, L.; Zheng, H.D.; Liu, Y.Y.; Yin, W.B.; Ma, W.G.; Zhang, L.; Jia, S.T. Optical Detection Technique Using Quartz-Enhanced Photoacoustic Spectrum. *Int. J. Thermophys.* **2015**, *36*, 1297–1304. [CrossRef]
5. Dumitras, D.C.; Petrus, M.; Bratu, A.M.; Popa, C. Applications of Near Infrared Photoacoustic Spectroscopy for Analysis of Human Respiration: A Review. *Molecules* **2020**, *25*, 1728. [CrossRef]
6. Helander, P.; Lundstrom, I.; Mcqueen, D. Light-Scattering Effects in Photoacoustic Spectroscopy. *J. Appl. Phys.* **1980**, *51*, 3841–3847. [CrossRef]
7. Mao, X.F.; Zheng, P.C.; Wang, X.F.; Yuan, S.Z. Breath Methane Detection Based on All-Optical Photoacoustic Spectrometer. *Sens. Actuators B* **2017**, *239*, 1257–1260. [CrossRef]
8. Gong, Z.F.; Chen, K.; Yang, Y.; Zhou, X.L.; Yu, Q.X. Photoacoustic Spectroscopy Based Multi-Gas Detection Using High-Sensitivity Fiber-Optic Low-Frequency Acoustic Sensor. *Sens. Actuators B* **2018**, *260*, 357–363. [CrossRef]
9. Yang, T.H.; Chen, W.G.; Zhang, Z.X.; Lei, J.L.; Wan, F.; Song, R.M. Multiple Reflections Enhanced Fiber-Optic Photoacoustic Sensor for Gas Micro-Leakage. *Opt. Express* **2021**, *29*, 2142–2152. [CrossRef]
10. Zhang, C.Z.; Yang, Y.H.; Tan, Y.Z.; Ho, H.L.; Jin, W. All-Optical Fiber Photoacoustic Gas Sensor with Double Resonant Enhancement. *IEEE Photonics Technol. Lett.* **2018**, *30*, 1752–1755. [CrossRef]
11. Chen, K.; Yu, Z.H.; Yu, Q.X.; Guo, M.; Zhao, Z.H.; Qu, C.; Gong, Z.F.; Yang, Y. Fast Demodulated White-Light Interferometry-Based Fiber-Optic Fabry-Perot Cantilever Microphone. *Opt. Lett.* **2018**, *43*, 3417–3420. [CrossRef] [PubMed]
12. Chen, K.; Zhang, B.; Guo, M.; Chen, Y.W.; Deng, H.; Yang, B.L.; Liu, S.; Ma, F.X.; Zhu, F.; Gong, Z.F.; et al. Photoacoustic Trace Gas Detection of Ethylene in High-Concentration Methane Background Based on Dual Light Sources and Fiber-Optic Microphone. *Sens. Actuators B* **2020**, *310*, 127825. [CrossRef]
13. Kauppinen, J.; Wilcken, K.; Kauppinen, I.; Koskinen, V. High Sensitivity in Gas Analysis with Photoacoustic Detection. *Microchem. J.* **2004**, *76*, 151–159. [CrossRef]
14. Karioja, P.; Keranen, K.; Kautio, K.; Ollila, J.; Heikkinen, M.; Kauppinen, I.; Kuusela, T.; Matveev, B.; Mcnie, M.E.; Jenkins, R.M.; et al. LTCC Based Differential Photo Acoustic Gas Cell for ppm Gas Sensing. *Proc. SPIE* **2010**, *7726*, 77260H.
15. Giacomo, P. The Michelson Interferometer. *Microchim. Acta* **1987**, *3*, 19–31. [CrossRef]
16. Naumann, H.; Schröder, G.; Löffler-Mang, M. *Handbook of Components in Optics: Fundamentals, Materials, Devices, Measurement Techniques*, 7th ed.; Hanser: Munich, Germany, 2014; pp. 403–413.
17. Lebreton, A.; Abram, I.; Braive, R.; Sagnes, I.; Robert-Philip, I.; Beveratos, A. Theory of Interferometric Photon-Correlation Measurements: Differentiating Coherent from Chaotic Light. *Phys. Rev. A* **2013**, *88*, 013801. [CrossRef]
18. Tsushima, A. Measurement of Neutral Gas Using Dispersion Characteristics of Sound Waves. *Jpn. J. Appl. Phys.* **2006**, *45*, 8141–8144. [CrossRef]
19. Tonogaki, T.; Ohno, N.; Takamura, S.; Tsushima, A. Sound Wave Propagation in Gases at Low Pressure. *Plasma Phys.* **2003**, *669*, 113–116.
20. Martin, R.B. Relative Humidity. *J. Chem. Educ.* **1999**, *76*, 1081–1082. [CrossRef]
21. Jones, F.E. The Refractivity of Air. *J. Res. Natl. Bur. Stand.* **1981**, *86*, 27–32. [CrossRef]

22. Bonsch, G.; Potulski, E. Measurement of the Refractive Index of Air and Comparison with Modified Edlen's Formulae. *Metrologia* **1998**, *35*, 133–139. [CrossRef]
23. Engineering Metrology Toolbox—Refractive Index of Air Calculator—Documentation. Available online: https://emtoolbox.nist.gov/Wavelength/Documentation.asp#IndexofRefractionofAir (accessed on 11 April 2023).
24. Hoffmann, M. Photoacoustic Interferometry for Gas Detection. Ph.D. Dissertation, Technical University of Munich, Munich, Germany, 2021.
25. Brampton, W.; Young, J.D. Lung-Volume, Pressure, Flow, and Density Relationships during Constant-Flow Ventilation in Dogs. *J. Appl. Physiol.* **1993**, *74*, 197–202. [CrossRef] [PubMed]
26. Zhao, F.; Sun, D.B.; Zhu, R.; Yang, L.Z. Effect of Shrouding Gas Parameters on Characteristics of Supersonic Coherent Jet. *Metall. Mater. Trans. B* **2017**, *48*, 1807–1816. [CrossRef]
27. Wang, S.; Hoffmann, M.; Yetisen, A.K.; Wang, K.; Brändle, F.; Kurz, W.; Jakobi, M.; Zhou, Q.; Koch, A.W. Optical Interferometer-Based Methods for Photoacoustic Gas Sensing: A Review. *Appl. Spectrosc. Rev.* **2023**, *58*, 1–40. [CrossRef]
28. Speed of Sound in Various Materials. Available online: https://www.rfcafe.com/references/general/velocity-sound-media.htm (accessed on 11 April 2023).
29. Solids and Metals—Speed of Sound. Available online: https://www.engineeringtoolbox.com/sound-speed-solids-d_713.html (accessed on 11 April 2023).
30. Air—Density, Specific Weight and Thermal Expansion Coefficient vs. Temperature and Pressure. Available online: https://www.engineeringtoolbox.com/air-density-specific-weight-d_600.html (accessed on 11 April 2023).
31. Air—Speed of Sound vs. Temperature. Available online: https://www.engineeringtoolbox.com/air-speed-sound-d_603.html (accessed on 11 April 2023).
32. Zhao, X.B.; Zhou, H.; Chen, H.M.; Wang, Y.F. Domain Decomposition for Large-Scale Visco-acoustic Wave Simulation Using Localized Pseudo-Spectral Method. *IEEE Trans. Geosci. Electron.* **2021**, *59*, 2666–2679. [CrossRef]
33. Gong, X.F.; Du, Q.Z.; Zhao, Q.; Guo, C.F.; Sun, P.Y.; Zhang, J.L.; Tian, Z.P. Pseudo-Analytical Finite-Difference Elastic-Wave Extrapolation Based on the K-Space Method. *Geophysics* **2018**, *83*, T1–T14. [CrossRef]
34. Xu, X.M. *Acoustic Foundation*, 1st ed.; Scientific Publisher: Beijing, China, 2003; pp. 131–134.
35. Density of Air. Available online: https://en.wikipedia.org/wiki/Density_of_air#cite_note-SInote01-13 (accessed on 11 April 2023).
36. Speed of Sound—Online Calculator. Available online: https://www.engineeringtoolbox.com/speed-sound-d_519.html (accessed on 11 April 2023).
37. Anderson, C.V.D.R.; Tamma, K.K. An Overview of Advances in Heat Conduction Models and Approaches for Prediction of Thermal Conductivity in Thin Dielectric Films. *Int. J. Numer. Methods Heat Fluid Flow* **2004**, *14*, 12–65. [CrossRef]
38. Quartz—Density—Heat Capacity—Thermal Conductivity. Available online: https://material-properties.org/quartz-density-heat-capacity-thermal-conductivity/?utm_content=cmp-true (accessed on 11 April 2023).
39. Metals and Alloys—Densities. Available online: https://www.engineeringtoolbox.com/metal-alloys-densities-d_50.html (accessed on 11 April 2023).
40. Efremov, V.P.; Ivanov, M.F.; Kiverin, A.D.; Yakovenko, I.S. Shock-Wave Processes Evolution in Fused Quartz Under Intense Energy Action. *J. Phys. Conf. Ser.* **2016**, *774*, 012119. [CrossRef]
41. Material: Aluminum. Available online: http://www.mit.edu/~6.777/matprops/aluminum.htm (accessed on 11 April 2023).
42. Muldiani, R.F.; Hadiningrum, K.; Pratama, D. Experiments for Determining the Thermal Conductivity of Brass and 304 Stainless Steel with Direct Temperature Measurement Techniques Using Lorenz Number as Validation. In Proceedings of the 2nd International Seminar of Science and Applied Technology (ISSAT 2021), Bandung, Indonesia, 12 October 2021.
43. Material: Pyrex Glass. Available online: http://www.mit.edu/~6.777/matprops/pyrex.htm (accessed on 11 April 2023).
44. Peng, L. Sound Absorption and Insulation Functional Composites. In *Advanced High Strength Natural Fibre Composites in Construction*, 1st ed.; Fan, M.Z., Fu, F., Eds.; Elsevier: Amsterdam, The Netherland, 2017; pp. 333–373.
45. Igarashi, J. The Determination of Sound Absorption Coefficient. *J. Phys. Soc. Jpn.* **1950**, *5*, 249–253. [CrossRef]
46. Jakub, P.; Grzegorz, M. Noise Variance Estimation Based on Knowledge of Noise Reduction Coefficient. In *Advanced Materials Research*, 1st ed.; Tan, H.H., Ed.; Trans Tech Publications: Zurich, Switzerland, 2012; Volume 340, pp. 149–155.
47. Hassanzadeh, S.; Hasani, H.; Zarrebini, M. Analysis and Prediction of the Noise Reduction Coefficient of Lightly-Needled Estabragh/Polypropylene Nonwovens Using Simplex Lattice Design. *J. Text. Inst.* **2014**, *105*, 256–263. [CrossRef]
48. Akseli, I. The Application of Aluminum Foam for the Heat and Noise Reduction. Master's Dissertation, Izmir Institute of Technology, Izmir, Turkey, 2005.
49. Jafar, N.A.; Ooi, L.E.; Mazlan, A.Z.A.; Seng, K.H.C.; Tan, J.M. The Evaluation of Deviation in Sound Absorption Coefficient for Micro—Perforated Panel. In Proceedings of the IOP Conference Series: Materials Science and Engineering, Batu Ferringhi, Malaysia, 2 December 2019.
50. Sound—Room Absorption Coefficients. Available online: https://www.engineeringtoolbox.com/accoustic-sound-absorption-d68.html (accessed on 11 April 2023).
51. Sikora, J.; Turkiewicz, J. Sound Absorption Coefficients of Granular Materials. *Mech. Control* **2010**, *29*, 149–157.
52. Noise Reduction Coefficient (NRC). Available online: https://svetlanaroit.files.wordpress.com/2009/11/visual_values2.pdf (accessed on 11 April 2023).

53. Cheng, G. Numerical Simulation, Optimization Design and Characteristic Analysis of Photoacoustic Gas Detection Device. Ph.D. Dissertation, University of Science and Technology of China, Hefei, China, 2019.
54. Yang, T. Study on Dual Resonance and Multi-Path Photoacoustic Spectroscopy for Characteristic Gases Measurement of Power Transformers. Ph.D. Dissertation, Chongqing University, Chongqing, China, 2021.
55. Liu, Y. Optimization of Photoacoustic Cell in Photoacoustic Spectroscopy Methane Gas Detection System. Master's Dissertation, Shijiazhuang Tiedao University, Shijiazhuang, China, 2021.
56. Specific Heat of Common Substances. Available online: https://www.engineeringtoolbox.com/specific-heat-capacity-d_391.html (accessed on 11 April 2023).
57. Jin, H.W.; Xie, P.H.; Hu, R.Z.; Huang, C.C.; Lin, C.; Wang, F.Y. Design of NO_2 Photoacoustic Sensor with High Reflective Mirror Based on Low Power Blue Diode Laser. *Chin. Phys. B* **2020**, *29*, 060701. [CrossRef]
58. Schjolberg-Henriksen, K.; Schulz, O.; Ferber, A.; Moe, S.; Lloyd, M.; Muller, G.; Suphan, K.H.; Wang, D.T.; Bernstein, R.W. Sensitive and Selective Photoacoustic Gas Sensor Suitable for High-Volume Manufacturing. *IEEE Sens. J.* **2008**, *8*, 1539–1545. [CrossRef]
59. Chen, X.; Zhou, C.M.; Fan, D.; Qian, L.; Pang, Y.D.; Wei, C.; Zhao, C.G.; Liang, S.J.; Li, Y.X. Modified Frequency-Shifted Interferometer: Encoding Wavelength into Phase. *Chin. Opt. Lett.* **2020**, *18*, 101203. [CrossRef]
60. Wang, S.C.; Chen, W.G. A Large-Area and Nanoscale Graphene Oxide Diaphragm-Based Extrinsic Fiber-Optic Fabry-Perot Acoustic Sensor Applied for Partial Discharge Detection in Air. *Nanomaterials* **2020**, *10*, 2312. [CrossRef] [PubMed]
61. Gong, Z.F.; Chen, K.; Chen, Y.W.; Mei, L.; Yu, Q.X. Integration of T-Type Half-Open Photoacoustic Cell and Fiber-Optic Acoustic Sensor for Trace Gas Detection. *Opt. Express* **2019**, *27*, 18222–18231. [CrossRef]
62. Guo, M.; Chen, K.; Yang, B.L.; Zhang, G.Y.; Zhao, X.Y.; Li, C.X. Miniaturized Anti-Interference Cantilever-Enhanced Fiber-Optic Photoacoustic Methane Sensor. *Sens. Actuators B* **2022**, *370*, 132446. [CrossRef]
63. Sampaolo, A.; Patimisco, P.; Giglio, M.; Zifarelli, A.; Wu, H.P.; Dong, L.; Spagnolo, V. Quartz-Enhanced Photoacoustic Spectroscopy for Multi-Gas Detection: A Review. *Anal. Chim. Acta* **2022**, *1202*, 338894. [CrossRef]